

**Synthesis and characterisation of Au/TiO₂ composites
for plasmon-enhanced visible light driven photocatalytic
degradation of reactive orange 16 dye**

by

Jenny Chansa Lumbala

**Dissertation submitted in fulfilment of the requirements for the Master
degree**

Master of Applied Science: Chemistry

in the Faculty of Applied Sciences

at the Cape Peninsula University of Technology

Supervisor: Dr Thandekile Mthethwa

Co-Supervisor: Dr Francois Wewers

Bellville

Date submitted (August 2019)

CPUT copyright information

The dissertation/thesis may not be published either in part (in scholarly, scientific or technical journals), or as a whole (as a monograph), unless permission has been obtained from the University

DECLARATION

I, **Jenny Chansa Lumbala**, declare that the contents of this dissertation/thesis represent my own unaided work and that the dissertation/thesis has not previously been submitted for academic examination towards any qualification. Furthermore, it represents my own opinions and not necessarily those of the Cape Peninsula University of Technology.

Signed

Date

ABSTRACT

Photocatalysis is one of the methods that have gained popularity for degradation of organic pollutants in water. Metal oxides, such as ZnO, Fe₂O₃, and TiO₂ are considered to be good and efficient photocatalysts. TiO₂, in particular, has been the most investigated because it is naturally abundant, non-toxic and stable. However, the wide band gap of TiO₂ (3.2 eV), make TiO₂ only to absorb UV light. For this reason, plasmon enhanced-photocatalysis has emerged as one of the appealing processes to achieve visible light utilization by TiO₂. This process exploits the Localized Surface Plasmon Resonance (LSPR) of the metal nanoparticles such as gold to harvest the visible light and bring about photocatalytic process. LSPR is the effect of the oscillation of electrons in noble metals when they are in contact with light. Due to the LSPR phenomena, noble metals are able to increase the lifetime of the charge carriers and increase electron/hole generation semiconductors photocatalysts under visible light.

In this study, TiO₂ was coupled with gold nanoparticles in order to facilitate visible light absorption and to improve the photocatalytic performance. Gold nanoparticles (nanospheres and nanorods) were synthesised using the Turkivich and seed mediated methods. These were characterised by UV-visible spectrophotometry, transmission electron microscopy (TEM) and scanning electron microscopy (SEM) for optical properties, size and morphology. The concentration of the as prepared gold samples was measured using the inductively coupled plasma optical emission spectrometry (ICP-OES). Gold nanospheres and gold nanorods were loaded into TiO₂ using the nucleation and growth method to obtain the Au/TiO₂ plasmonic composites. To investigate to effect of the gold size, two AuNRs samples with different aspect ratios (1.9 and 3.4) were prepared and used to form the nanocomposites with TiO₂. Another Au/TiO₂ composite sample was prepared by loading AuNS to compare the behaviour of the two shapes. The characterisation results of these samples from the transmission electron microscopy TEM and SEM confirmed the expected shapes (spheres and rods) and the formation of the nanocomposites. The energy dispersive spectroscopy (EDS) results showed the presence of the all the expected elements in the composites materials, further confirming the successful synthesis of the Au/TiO₂ composites. The absorption spectra of the prepared nanocomposites showed the plasmonic peaks of the gold nanoparticles in the visible region, which also confirmed the formation of the composite materials.

The photocatalytic performance of the photocatalysts was investigated for the degradation of reactive orange 16. From the results obtained in this study, it was found that the photocatalysts loaded with AuNRs gave higher photodegradation efficiencies compared to the one loaded with

AuNS. The photocatalytic efficiency was found to increase with an increase on the aspect ratio of the AuNRs. For AuNRs (1.9) the achieved efficiency was 84.56 % and 86.65 % for AuNRs (3.4). Meanwhile, direct photolysis did not have an effect on the photodegradation of Reactive Orange 16 (RO 16). The combined effect of AuNRs and AuNS showed a drastic improvement on the photocatalytic efficiency and the rates of the process which was attributed to the synergistic effects of the transverse and the longitudinal plasmons peaks of both nanospheres and nanorods. The photocatalyst prepared with the mixed nanospheres and nanorods gave an efficiency of up to 90.15 % for the 1:1 ratio at 60 min reaction time.

A number of reaction parameters were investigated for their effect on the photodegradation efficiency including: pH, Au content, and temperature. The photocatalytic degradation of RO 16 was very slow in very acidic (pH 2.5) and very basic conditions (pH 11.5). The highest degradation efficiency was achieved at pH of about 6.7. Furthermore, the rate of degradation also increased with an increase in temperature from 15 °C to 30 °C due to the reduction of the activation energy. The increase in Au loading from 0.1 wt % to 0.2 wt % increased the photocatalytic performance of the catalyst from 56.29 % to 86.65 %. However, further increase in gold loading blocked the light penetration and hence, caused a decrease on the efficiency to 66.35 %.

ACKNOWLEDGEMENTS

I wish to thank:

- Dr Thandekile Mthethwa, it's rare to find an accommodating supervisor, always so willing to listen, guide, encourage and support me. This thesis would not be possible without you.
- Dr Francios Wewers, who made sure things were kept simple and gave me space in is research team.
- The chief Lab Technician Mrs Zandile Mthembu and other lab staff or their support, who facilitated the use of the instruments in the laboratory
- My mother Francoise Safi Kungwa, I hope I made you proud and your prayers were eventually answered.
- My siblings, I am sincerely grateful for support, encouragement and for believing in me
- My friends and Laboratory colleague, thank you all.
- I wish to thank water research commission (WRC) for funding the project.

DEDICATION

To my lovely parents: Henri Mukonde Chansa and Francoise Safi Kungwa.

TABLE OF CONTENTS

DECLARATION	I
ABSTRACT	II
ACKNOWLEDGEMENTS	IV
DEDICATION	V
TABLE OF CONTENTS	VI
GLOSSARY	IX
LIST OF FIGURES	X
LIST OF TABLE	XII
CHAPTER 1	
1. INTRODUCTION AND BACKGROUND	1
1.1. Background	1
1.2. Problem Statements	3
1.3. Research Questions	3
1.4. Objectives of the Research	3
1.5. Significance of the Research	4
1.6. Research Assumptions	4
1.7. Limitations of the study	4
1.8. Thesis Outline	5
CHAPTER 2	
LITERATURE REVIEW	6
2.1 Overview on catalysis	6
2.2 Heterogeneous photocatalysis	7
2.3 Heterogeneous photocatalysis and water purification	7
2.4 Semiconductor photocatalytic materials	8
2.5 TiO ₂ crystalline structure and photocatalyst	9
2.6 Strategies for improving photocatalytic properties of TiO ₂	11
2.6.1. Non-metal doping	11

2.6.2	. Transition metal doping	12
2.6.3	Metal oxide/ TiO ₂	12
2.7	Plasmon-enhanced photocatalysis	13
2.7.1	. Surface plasmon resonance of the gold nanoparticles	13
2.7.2	. Plasmon enhanced mechanisms	14
2.8	Methods for synthesis for gold nanoparticles	16
2.8.1	. Turkevich method	16
2.8.2	. Brust method	16
2.8.3	Seed mediated method	16
2.9	. Au/TiO ₂ composites in photocatalysis	17
2.10.	Synthesis of Au/TiO ₂ nanocomposites	18
2.10.1	Impregnation and precipitation method	18
2.10.2	Green synthesis method	18
2.10.3	Self-assembly method	18
2.10.4	Hydrothermal method	19

CHAPTER 3

MATERIALS AND METHODS	20
3.1 .Materials	20
3.1.1. Reagents used for the synthesis of Au Nanoparticles and Au/TiO ₂ nanocomposites	20
3.2. Equipment	20
3.2.1. X-ray diffraction (XRD)	20
3.2.2. Ultraviolet-Visible spectroscopy (UV-VIS)	21
3.2.3. Transmission electron microscopy	22
3.2.4. Scanning electron microscopy	22
3.2.5. Fourier transform infrared spectroscopy	22
3.2.6 Inductively Coupled Plasma—Optical Emission Spectroscopy (ICP-OES)	23
3.3 . Synthesis of gold nanoparticles	23

3.3.1. Synthesis of gold nanorods	23
3.3.2. Synthesis of gold nanospheres	24
3.4 . Synthesis of TiO ₂ nanoparticles	24
3.5 Synthesis of Au/TiO ₂ composites	25
3.6 . Photocatalytic degradation of reactive orange 16	26
CHAPTER 4	
CHARACTERISATION OF THE GOLD NANOPARTICLES AND AU/TIO₂ COMPOSITES	28
4.1 Quantification and properties of the gold nanoparticles	28
4.2 Microscopic analysis of Au and Au/TiO ₂ nanocomposites	29
4.3 Optical properties of Au nanoparticles, TiO ₂ and Au/TiO ₂ nanocomposites	33
4.4 Structural properties of Au nanoparticles, TiO ₂ and Au/TiO ₂ nanocomposites	34
CHAPTER 5	
PHOTOCATALYTIC DEGRADATION OF REACTIVE ORGANGE 16	37
5.1 Shape and size effect on the photodegradation and decolourization of RO 16.	38
5.2 Determination of the electrical Energy Efficiency per order (E _{EO})	43
5.3 Synergistic plasmonic effect of nanospheres and nanorods on the degradation of RO16 .	44
5.6 Reusability of the photocatalyst	47
CHAPTER 6	
EFFECT OF OPERATIONAL PARAMETERS ON THE PHOTOCATALYTIC DEGRADATION OF RO 16	49
6.1 Effect of Au loading in Au/TiO ₂ nanocomposites	49
6.2 Effect of pH on the degradation of RO16	50
6.3 Effect of temperature	53
CHAPTER 7	
CONCLUSIONS AND RECOMMENDATIONS	55
7.1 Conclusions	55
7.2 Recommendations	56
REFERENCES	57

GLOSSARY

AOPs	Advanced oxidation processes
AOTs	Advanced oxidation techniques (Technologies)
Au	Gold
AuNPs	Gold nanoparticles
AuNS	Gold nanosphere
AuNRs/ TiO₂	Gold Nanorods Titanium oxide
AuNS/TiO₂	Gold nanosphere titanium oxide
CB	Conduction band
VB	Valence band
UV-VIS	Ultraviolet-Visible
h⁺	Hole or electron pair
e⁻	Electron
eV	Electron volt
SPR	Surface Plasmon Resonance
LSPR	Localized Surface Plasmon Resonance
SHE	Standard hydrogen electrode
NHE	Normal Hydrogen electrode
O₂[•]	Oxygen radical anion
HO[•]	Hydroxyl radical
R²	Correlation coefficient
C_o	Initial concentration
C_t	Concentration at time (t)
V	Volume

LIST OF FIGURES

- Figure 2.1** Representation of the semiconductor band gap energy and the positioning edge with a potential scale against the normal hydrogen electrode (NHE)
- Figure 2.2** Schematic illustration of the photocatalytic process
- Figure 2.3** Schematic illustration of AuNS interaction with the electromagnetic field of visible light
- Figure 2.4** Schematic illustration of AuNRs interaction with the electromagnetic field of visible light
- Figure 2.5** Schematic illustrations of the charge transfer mechanism between plasmon metals and semiconductors under visible light
- Figure 3.1** schematic illustration of visible region wheel colour
- Figure 3.2** Schematic illustration of seed-mediated method for synthesis of Au nanorods (AuNRs).
- Figure 3.3** Schematic illustration of the synthesis of TiO₂ nanoparticles from titanium butoxide
- Figure 3.4** Schematic illustration of the synthesis of Au/TiO₂
- Figure 3.5** Schematic illustration of a typical set-up for testing of photocatalytic activity of Au/TiO₂ composites.
- Figure 4.1** TEM images (A) NS, (B) Au (1.9) NRS, (C) Au (3.4) NRs, (D) AuNS/TiO₂, (E) AuNRs (1.9)/ TiO₂ and (F) AuNRS (3.4)/TiO₂
- Figure 4.2** SEM images of AuNS/TiO₂, (A), AuNRs/TiO₂ (B) Au/TiO₂, nanocomposites and the corresponding EDS (C).
- Figure 4.3** UV-Visible spectra (A) of AuNS, Au nanorods (1.9), gold nanorod (3.4) and (B) AuNS/TiO₂, AuNRs (1.9)/TiO₂, AuNRs/TiO₂ and TiO₂.
- Figure 4.4** XRD patterns of (a) TiO₂ and (b) AuNRs/TiO₂ nanocomposites and (c) AuNS/TiO₂
- Figure 4.5** Fourier Transform Infrared (FTIR) spectrum of Au/TiO₂ nanocomposites.
- Figure 5.1** Absorption spectra of the change in concentration of RO 16 [C=20 ppm, Ccat= 0.2 g/L, pH= 6.7] using AuNRs(3.4)/TiO₂ (A), AuNRs(1.9)/TiO₂ (B). And AuNS/TiO₂ (C) as catalysts .
- Figure 5.2** Degradation efficiency of RO 16 [C=20 ppm, Ccat= 0.2 g/L, pH= 6.7] AuNRs(3.4)/TiO₂, AuNRs(1.9)/TiO₂. AuNS/TiO₂, no catalyst and TiO₂.
- Figure 5.3** Kinetic plot of the degradation of RO 16 [C=20 ppm, Ccat= 0.2 g/L, pH=

6.7, power= 300W] AuNRs(3.4)/TiO₂, AuNRs(1.9)/TiO₂. AuNS/TiO₂, no catalyst and TiO₂.

Figure 5.4 (A) Mixed shapes, AuNRs and AuNS photodegradation efficiency (B) first order kinetic of the mixed shapes effect the degradation of RO 16 [C=20 ppm, Ccat= 0.2 g/L, pH= 6.7, power= 300W] AuNRs(3.4)/TiO₂, AuNRs(1.9)/TiO₂. AuNS/TiO₂, no catalyst and TiO₂.

Figure 5.5 Photodegradation efficiency reusability test for of RO 16 [C=20 ppm, Ccat= 0.2 g/L, pH= 6.7, power= 300W] AuNRs(3.4)/TiO₂, AuNRs(1.9)/TiO₂. AuNS/TiO₂, no catalyst and TiO₂

Figure 6.1 Effect of Au loading onto Au/TiO₂ on the photocatalytic degradation efficiency of RO 16. [C=20 ppm, Ccat= 0.2 g/L, pH= 6.7, power= 300W]

Figure 6.2 Degradation efficiency percentage of the effect of pH on RO 16 decolourisation, and degradation [C=20 ppm, Ccat= 0.2 g/L, pH= 6.7, power= 300W]

Figure 6.3 Effect of temperature on the photocatalytic degradation efficiency of RO 16 [C=20 ppm, Ccat (Au/TiO₂)= 0.2 g/L, pH= 6.7, power= 300W]

LIST OF TABLE

- Table 2.1** Comparison of the three TiO₂ crystalline structures
- Table 2.2** Summary of previous studies done on the degradation of organic dyes with Au/TiO₂.
- Table 4.1** Concentration, extinction coefficients, wavelength and the number of particles per atoms of gold nanorods and spheres
- Table 4.2** XRD data of Au/TiO₂ nanocomposites
- Table 5.1** General characteristics of reactive orange
- Table 5.2** Photodegradation efficiency and kinetic properties of RO16 using the TiO₂ AuNS/TiO₂ AuNRs (1.9)/TiO₂ and AuNRs (3.4)/TiO₂ composites
- Table 5.3** Summary of varying nanospheres and nanorods ratios on the degradation of RO16
- Table 6.1** Summary results of the photodegradation of RO 16 of the effect of Au loading onto Au/TiO₂
- Table 6.2** summary of the photodegradation data with a change in pH using Au/TiO₂ nanocomposites with 20 pm as the concentration of RO 16 with catalyst load of 0.2 g/L.

CHAPTER 1

1. INTRODUCTION AND BACKGROUND

This chapter contains the background of this study, scope and significance, the aim and project objectives and as well as the thesis outline..

1.1. Background

The textile industry is one of the largest consumers of water, and therefore, generates large amounts of effluent wastewater (Ajmal et al., 2014). The textile industry uses a vast array of chemicals and ever increasing volumes of water. These chemicals range from de-aerating agents, levelling agents, soaping agents, antifoaming, wetting agents, softness, oil and grease release hydrocarbons, thickeners, alkali and acids, peroxide stabilisers and scavengers, etcetera (Roy Choudhury, 2018, Holkar et al., 2016). According to reports, about 200 L of water per 1 Kg of textile fabric is required per day (Latha et al., 2018, Holkar et al., 2016). Wastewater generated from the textile industry is coloured, which indicates the presence of dye pollutants (Haroun & Idris, 2009). The complexity of the dye mix and the concomitant effluent ensures the dye effluent mix is difficult to remediate (Roy Choudhury, 2018). The textile industry uses different dyes during the dyeing and the printing processes, over 700 000 tons of synthetic dyes are produced every year, and around 1000 tons of these dyes are discharged in the water streams (Ajmal et al., 2014). Therefore, the biggest challenge for wastewater treatment plants in the textile industry is the colour removal. Dyes are mutagenic and carcinogenic, and they are deadly to some aquatic life due to the formation of toxic breakdown products and increase the chemical oxygen demand in the water (Roy Choudhury, 2018, Ananthashankar, 2013; Zaharia & Suteu, 2012). Textile dyes are classified based on their structure, source and fibre type such as reactive dye, Indigo, direct dyes and disperse dyes (Selvakumar et al., 2012). Azo dyes constitute more than 50 % of all the synthetic dyes produced (Haroun & Idris, 2009). They are very stable because of the aromatic group attached to one or more (-N=N-) amine functional groups. The stable and intense colour makes azo dyes a huge concern for the environment since this colour reduces the transparency and the quality of water, which causes a plethora of environmental issues (Holkar et al., 2016; Lu et al., 2010).

Current treatment techniques include adsorption, chlorination, membrane filtration and clarification, UV-treatment and biological degradation (Sharma & Bhattacharya, 2016). Most of these techniques suffer drawbacks, for example, the adsorption technology only succeeds in

transferring the target contaminant from the aqueous phase onto a solid and hence, generates secondary waste in the spent adsorbent (Sharma & Bhattacharya, 2016; Zhang et al., 2006). Membrane technology suffers from membrane fouling, while biological treatment requires specialized microbes that can survive the toxic mix that constitutes the effluent water (Sharma & Bhattacharya, 2016). The advanced oxidative technologies (AOTs) aim to harness the superior oxidizing power of radicals generated during the processes to enable water purification (Chong et al., 2010). Heterogeneous catalysed photodegradation is of particular interest when the catalyst can significantly reduce the overall cost (energy and time) of the treatment process and can be recovered and recycled (Lee & Park, 2013).

Several photocatalysts have been developed for photodegradation, among this titanium dioxide (TiO_2) has been given more attention due to its non-toxic nature and high stability. TiO_2 (band gap 3.2 eV) absorbs the ultraviolet (UV) light to generate reactive holes (h^+), which are responsible for the oxidation of soluble organics. Research trends have attempted to improve the photocatalytic properties of TiO_2 by incorporating plasmonic metals such as Au, Ag and Cu other transition metals (Ibhadon & Fitzpatrick, 2013). Plasmonic photocatalysis has been investigated not only reduce the band gap of TiO_2 but also to increase the photocatalytic activity of TiO_2 . The ultimate goal is to extend the band gap of TiO_2 into the visible region for possible utilization of abundant solar energy. By tuning the shape and size and the surrounding of noble metals it was found that TiO_2 was able to increase its photocatalytic activities (Gołębiewska et al., 2016). Research on the development of visible-light-active photocatalysts is more desirable to ensure the usage of the entire spectrum of the abundant solar energy (Bora & Mewada 2017). Coupling TiO_2 semiconductor with gold nanoparticles (AuNPs) is expected to enhance and broaden the absorption of light in the visible spectrum (Liu et al. 2017). So far, there have been attempts to incorporate gold nanoparticles into semiconductors for the degradation of organic dyes (Ayati et al. 2014). However, these studies have been focused on spherically-shaped AuNPs and less attention has been given to the rod-shaped counterparts. Therefore, in this work, the Localised Surface Plasmon Resonance (LSPR) effects of the gold nanorods (AuNRs) in combination with TiO_2 were investigated. Reactive Orange 16 was chosen as a model azo dye for the investigation of the photocatalytic activity of Au/ TiO_2 nanocomposites.

1.2. Problem Statements

Azo dyes are the main organic synthetic dye used in textile industries (Murciamesa, 2017, Singh & Arora, 2011). The presence of dyes in surface waters highlights the inability of conventional techniques to treat wastewater from dye industries. The high stability of azo dyes makes it difficult to degrade by biological processes (Latha et al., 2018, Karimi et al., 2014). Conventional methods for the treatment of azo dyes results in the formation of carcinogenic and toxic aromatic amines that pose a threat to the environment and human health (Ajmal et al., 2014). In view of the highlighted drawbacks, research has been devoted to exploiting the advantages of advanced oxidation techniques (AOT) for treatment of organic pollutants in wastewater. Photocatalysis has been proven to be effective in the degradation of azo dyes using solar energy (Rauf et al., 2011). However, the application of photocatalysis on a large scale is still significantly limited because of the rapid recombination of excited electrons and holes. Systematic research on the design of photocatalysts with limited electron/hole recombination is of importance in this field. Despite the many advantages of TiO_2 photocatalysts, the major drawback is that it absorbs only 5 % of the entire solar spectrum. (Bansa et al., 2009), limiting the use of solar energy in photocatalysis for wastewater treatment. Coupling TiO_2 with plasmonic nanoparticles is one of the strategies that can be used to extend the photocatalytic activity to the visible spectrum and the efficiency of TiO_2 . The visible spectrum is desirable because it represents about 45% of solar energy (Agegnehu et al., 2016).

1.3. Research Questions

- Can AuNRs enhance the photocatalytic efficiency of TiO_2 under visible light?
- Will surface plasmon resonance (SPR) induced mechanism of visible light photocatalysis in AuNRs compared to AuNS?
- How do parameters such as pH, temperature and loading of AuNPs affect the photocatalytic process?

1.4. Objectives of the Research

The main aim of this project was to synthesise and characterise visible light driven Au/ TiO_2 composite photo-catalyst and applied to the degradation of reactive orange 16 azo dye
In order to achieve the aim the following objectives were proposed:

- To synthesise and characterise gold nanoparticles (rods and sphere).
- To synthesise and characterise Au/TiO₂ composites.
- To perform photocatalytic degradation of reactive orange 16 azo dye under visible light.
- To study the effect of shape and size of gold nanoparticles on the photocatalytic efficiency of the nanocomposite
- To study the effect of the AuNRs on the photocatalytic efficiency of the nanocomposites.
- To study the effect of reaction parameters such as pH, temperature and AuNPs loading.
- To evaluate the plasmon-enhanced mechanisms and kinetics.

1.5. Significance of the Research

The removal of organic dyes from textile effluents is a big challenge, organic dyes turn to cause serious environmental problems. Visible light photocatalysis offers a good opportunity to harvest solar energy for the treatment of organic dyes in industrial effluents. Therefore, a mechanistic understanding of the plasmon effects is very important for the design of highly effective photocatalysts for complete removal of organic dyes. The information obtained from this project will add valuable information to the design of the solar photocatalytic reactors and the availability of the more efficient visible light active photocatalyst.

1.6. Research Assumptions

Organic dyes in wastewater can be degraded using visible-light-active Au/TiO₂ photocatalysts.

- Au/TiO₂ composites will demonstrate visible light activity due to the surface plasmon resonance of gold.
- The photocatalytic efficiency of TiO₂ will be improved by the presence of plasmonic AuNRs through plasmon-enhanced mechanisms.
- The use of Au/TiO₂ as a photocatalyst will degrade the dye in the water to form less toxic products.

1.7. Limitations of the study

The synthesis and characterisation of visible light active photocatalyst based on AuNRs/TiO₂ were conducted in this project.

- This project focus was on the degradation of reactive orange dye 16 only.
- Photocatalysis experiments were performed with a suspended photocatalyst only.

1.8. Thesis Outline

Chapter 1; This chapter contains the background of this study, scope and significance, the aim and project objectives and as well as the thesis outline.

Chapter 2: Chapter two covers the literature review with a broad explanation of the topic of this project.

Chapter 3: This chapter explains the experimental procedures, materials and methods of characterization of the gold nanoparticles and Au/TiO₂ nanocomposites.

Chapter 4: This chapter presents the discussion on the structural and optical properties of the photocatalyst materials synthesised in this project.

Chapter 5: Chapter five elucidates the effect of shape and size of gold nanoparticles on the photocatalytic performance of the Au/TiO₂ nanocomposites.

Chapter 6: This chapter contains the investigation on conditions affecting the degradation of reactive orange 16 using Au/TiO₂ as a plasmon based photocatalyst.

Chapter 7: Conclusion of the whole study and present the recommendations for future research.

CHAPTER 2

LITERATURE REVIEW

This chapter contains the literature review with a broad explanation of the topic of this project.

2.1 Overview on catalysis

In 1850 Wilhelm proved that the rate of a chemical reaction depends on the concentration of the reactants (Wilhelm, 1850). William Ostwald (1882) changed Wilhelm's point of view by saying 'a catalyst cannot initiate a chemical change but can accelerate or reduce the speed of the reaction'. Later a catalyst was defined as a material that changes the chemical rate of the reaction without getting involved in the reaction, and do not affect the thermodynamic equilibrium of a reaction (Lindströma & Pettersson, 2003). Nowadays almost all the chemical reactions take place in the presence of a catalyst, some reactions cannot happen without a catalyst being present. Catalysis is applicable in many environmental pollution issues, such as in water purification and air purification; there are two types of catalyst, homogeneous catalyst and heterogeneous catalysts.

In homogeneous catalysis, the reactants and the catalyst are in the same physical phase. According to Michalska & Webster (1974), homogeneous catalysts have a better active site, all the metal atoms are available and the electronic and steric environment of the metal differs widely. However, the separation of the catalyst from the product after the reaction is very difficult and there exist the possibility of the decomposition of the catalyst by temperature (Michalska. & Webster, 1974). In heterogeneous catalysis the reactants and the catalyst are in a different phase, the catalyst is usually in a solid state and the reactants are mostly in liquid and gas state. The biggest advantages of the heterogeneous catalyst over homogeneous catalyst are that they can be easily synthesised, and they are easy to separate from the products after the reaction. Heterogeneous catalysts are the most widely used in industries, with the reaction taking place on the surface of the metal (Ranga, 2017). The rate of the reaction can be increased or decreased based on the principle given by Scholten (1985), which states that 'the rate of the reaction is increased when the energy barriers of the catalytic path are lower to the energy barriers of the nonanalytic path'.

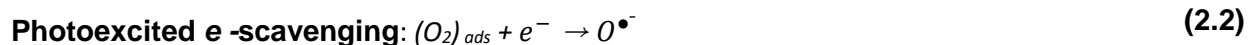
2.2 Heterogeneous photocatalysis

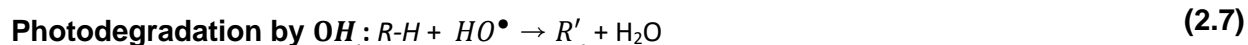
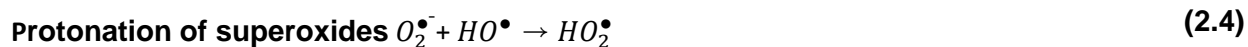
Heterogeneous photocatalysis is considered as a new advanced oxidation process. Fujishima & Honda (1972) discovered TiO₂ photocatalyst in 1972, for photochemical water splitting into hydrogen and oxygen. Heterogeneous photocatalysis has been applied in solar water splitting and water and air purification (Ibhadon & Fitzpatrick, 2013). It has demonstrated great potential in the treatment of wastewater and according to Herrmann in 1999, the reaction takes place the steps described below (Herrmann, 1999):

- The pollutants transfer from the solution onto the surface of the catalyst.
- Absorption of pollutants
- The reaction of adsorbed pollutants.
- Desorption of degradation products and separation of the photocatalyst.

2.3 Heterogeneous photocatalysis and water purification

A photocatalyst is defined as a material that is able to absorb light of a specific wavelength to generate electron-hole pairs (Lindströma & Pettersson, 2003). The structural properties of a photocatalyst such as high surface area, morphology, recyclability, band gap and stability are vital in a photocatalytic process (Khan et al., 2015). Photocatalysts are activated by light of appropriate energy equal to or higher than the band gap energy. The electrons are then promoted from the valence band (VB) to the conduction band (CB) leaving behind a hole (h⁺). The generated hole reacts with an HO[•] radical, which is highly reactive and capable of attacking the organic compounds. Adsorbed on the surface of the photocatalyst. The photocatalytic process involves the conversion of highly toxic pollutants to less toxic species or to CO₂ and H₂O. To utilise semiconductor photocatalysts for water purification, the following conditions to be met, the process should be performed at room temperature. Furthermore, total mineralization without secondary pollution, repetitive cycles and low costs for operations (Lee & Park.,2013). The mechanism of the electron-hole pair in the TiO₂ photocatalyst is postulated to be given by the following equations (Chong et al., 2010).





Equation 2.1 and 2.2 represent the exposure of TiO_2 to UV light in an aqueous medium, the photo-induced charge carriers in the conductive band (CB) take part in the reduction process, which reacts with dissolved oxygen in the air to produce superoxide radical anions ($O_2^{\bullet-}$). **Equation 2.3** shows the charge carriers in the VB diffuse to the TiO_2 surface and react with water molecules adsorbed, producing HO^\bullet (Lee and Park, 2013). The superoxide is either protonated or reduced to form H_2O_2 in **Equation 2.4 to 2.6**. The HO^\bullet radical is a major active species during the photocatalytic oxidation reaction (Xu et al., 2012). **Equations 2.7 to 2.8** depict the formation of dye intermediates, oxidation and reduction on the surface of TiO_2 .

2.4 Semiconductor photocatalytic materials

Metal oxides are of great interest in environmental remediation because of their ability to generate charge carriers when irradiated with the required amount of energy. Heterogeneous photocatalytic processes using semiconductors such as ZnO , TiO_2 , and Fe_3O_4 as photocatalysts are of great interest for the degradation of toxic organic pollutants because of their photocatalytic performances. The decomposition reaction of polluted materials is an oxidative reaction and depends on the valence band (VB) of the photocatalyst (Rostami-Vartooni et al., 2016). Therefore, the oxidation reaction is enhanced when the oxidative strength of the VB holes is high and there is a large positive number for standard electrode potential with respect to the standard hydrogen electrode (SHE) potential (Wang et al., 2017). **Figure 2.1** represents the band gap values of different semiconductors with respect to the normal hydrogen electrode (NHE). The band gap value differs from one semiconductor to another; hence, a careful selection of the material is of great importance.

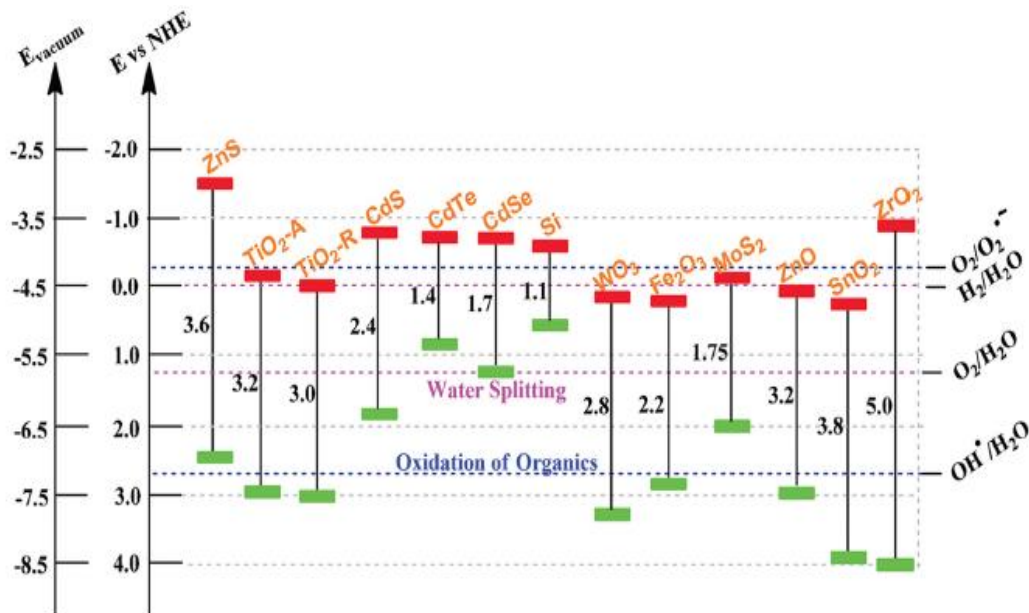


Figure 2.1: Representation of the semiconductor band gap energy and the positioning edge with a potential scale against the normal hydrogen electrode (NHE) (Wang et al., 2017).

The semiconductor is activated when it is bombarded with photons or energy equal or greater to the band gap causing the excitation of electrons from the VB to CB resulting in the formation of a hole (h^+) in the VB. These holes react with electron donors and acceptors that were absorbed on the surface of the semiconductor, leading to a redox reaction.

2.5 TiO₂ crystalline structure and photocatalyst

TiO₂ exists in three crystalline forms, viz. anatase, rutile and brookite. The three phases occur naturally and can be prepared in the laboratory (Di Paola et al., 2013). **Table 2.1** presents a comparison between anatase, brookite and rutile crystal structures. Brookite is usually formed as a by-product in the synthesis of rutile or anatase and it is the least studied or used of the three crystalline phases (Di Paola et al., 2013). It has an orthorhombic crystal system, with the Ti atom at the centre surrounded by oxygen atoms at the corners of the crystal cell. Rutile, on the other hand, is the most stable and has a tetragonal crystal structure, with TiO₆ octahedron with a slight distortion from the orthorhombic structure (Reyes-Coronado et al., 2008). Even though rutile has the most stable crystal structure at high temperature and high refractive index, it has a lower photocatalytic activity compared to anatase (Henderson, 2011). Anatase has a tetragonal structure like rutile; however, the TiO₆ distortion is larger for anatase as compared to rutile.

Anatase shows good photocatalytic activity and is kinetically stable at low temperatures (Reyes-Coronado et al., 2008).

Table 2. 1: Comparison of the three TiO₂ crystalline structures (Ali et al., 2018).

TiO ₂ , crystalline forms	Crystal structure	Band gap (eV)	Density g/cm ³	O-Ti-O bond angle (°C)	Lattice constant (nm)
Anatase	Tetragonal	3.2	3.79	77.7, 92.6	a=0.3784, c=0.9415 a=0.9184, b=0.5447,
Brookite	Tetragonal	3.13	3.99	77 to 105	c=0.5154
Rutile	Orthorhombic	3	4.13	81.2, 90	a=0.45936, c=0.29587

TiO₂ is photochemically stable, non-toxic and has a strong resistance against acids and alkalis (Lee and Park, 2013). **Figure 2.2** is a schematic representation of how TiO₂ functions as a photocatalyst. When TiO₂ is exposed to UV light in an aqueous medium, the photo-induced charge carriers in the conductive band (CB) take part in the reduction process, which react with dissolved oxygen from the air to produce superoxide radical anions (O₂^{•-}). The charge carriers in the valence (VB) diffuse to the TiO₂ surface and react with water molecules adsorbed, producing the HO[•] radical (Lee and Park, 2013). The HO[•] radical is a major active species during the photocatalytic oxidation reaction (Xu et al., 2012).

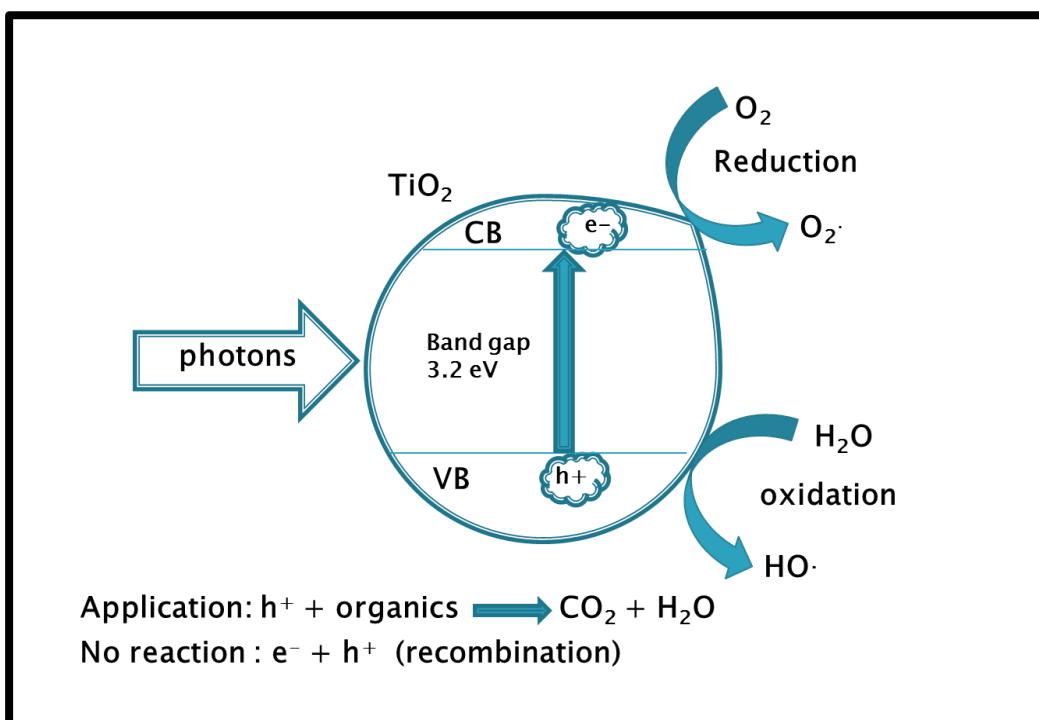


Figure 2.2: Schematic illustration of the photocatalytic process.

2.6 Strategies for improving photocatalytic properties of TiO₂

The wide band gap (3.2 eV) of TiO₂ restricts the optical absorption of TiO₂ in the ultraviolet (UV) region that encompasses less than 5 % of natural solar radiation activities (López-Vásquez et al., 2010), leading to the insufficient usage of solar energy. To improve the photocatalytic performance of TiO₂, different modification methods have been implemented to extend the band gap of TiO₂ from the UV to the visible region of the spectrum (Rostami-Vartooni et al., 2016). Metal and non-metal elemental doping have been extensively used for TiO₂ to expand its optical response to the visible light region (Ansari et al., 2016; Ashi, 2001). The main reason for adding dopants onto TiO₂ nanostructures is to reduce the band gap and to prevent rapid charge recombination. The different strategies for improving the photocatalytic activity of TiO₂ are discussed below.

2.6.1. Non-metal doping

There are numerous reports available on the non-metals doping of TiO₂, (Xu et al., 2008; Wang et al., 2012, Peichang et al., 2010, Di Valentin et al., 2005, Li et al., 2008). TiO₂ nanomaterials doped with non-metals have been regarded as second-generation photocatalysts. It has been shown that doping with non-metals such as C, F, B, S, Cl, N and Br can prevent the recombination of the electron and hole (Xu et al., 2008; Wang et al., 2012). More recently,

several researchers have reported improved non-metal-doped TiO₂ in particular with halogen atoms such as Cl, Br, and I, which showed high photocatalytic activity in the UV region as well as in the visible spectrum (Wang et al., 2012). Halogen doping was found to be effective due to the impurity states they have near the valence band edge (Peichang et al., 2010). The impurities created by anions induce localized occupied states in the TiO₂ band gap (Di Valentin et al., 2005). These localized states are responsible for the red shift of the TiO₂ adsorption band. In addition, the oxygen vacancies created by doping TiO₂ with anions can be account for the visible light photo-response of non-metal doped TiO₂ (Li et al., 2008).

2.6.2. Transition metal doping

Previous studies have shown that doping with transition metals improves the photocatalytic activity in the visible range (Yoong et al., 2009, Rauf et al., 2011, Araña et al., 2005). A number of transition metals such as Fe, Zn, Cr, Cu, Ni and V have been used to dope TiO₂ (Yoong et al., 2009, Rupa et al., 2007; Mikhani et al., 2009; Wu et al., 2016). Doping with these metals essentially reduces the recombination rate of photo-generated electron-hole pairs, hence, improving photocatalytic efficiency. Furthermore, transition metals result in the overlapping of the conduction band of TiO₂ with the *d*-orbital of the transition metal, which causes the reduction of the TiO₂ band gap (Yoong et al., 2009). Rauf and co-workers (2011) reported that the use of Cr³⁺ as a dopant in TiO₂ caused a reduction of the band gap by 2.0 eV and the recombination lifetime of the electron-hole pairs was also reduced from 89.3 ms (pure TiO₂) to 30 ms in the presence of Cr³⁺. Cu²⁺ ions have been reported to induce visible light photoactivity in TiO₂ by modifying its valence band due to the overlapping of the CB of TiO₂ and *d*-orbital of Cu²⁺ (Araña et al., 2005). Even though transition metals have shown positive results as dopants in metal oxide semiconductors, they have been reported to cause thermal instability for the anatase crystalline phase of TiO₂ (Ajmal et al., 2014).

2.6.3 Metal oxide/ TiO₂

Coupling two or more metal oxides can also result in the improvement of TiO₂ photocatalytic efficiency. This strategy creates impurities into the TiO₂ band gap leading in the reduction of the TiO₂ band gap (Perkgoz et al., 2011). For example, Fe₂O₃/TiO₂ nanocomposites were synthesised and used for the degradation of 2,4-dichlorophenoxyacetic acid, and a three times increase efficiency was reported in the presence of Fe₂O₃ compared to the pure TiO₂ (Lee et al., 2017). The improvement in the efficiency was attributed to the formation of a hetero-junction between TiO₂ and Fe₂O₃ nanoparticles, which led to the improvement of charge transfer and minimization of electron-hole pair recombination (Lee et al., 2017). It was also reported that

Fe₂O₃ increased the selectivity of TiO₂ during photodegradation of organic pollutants (Xia & Yin, 2013; Kwiatkowski et al., 2017).

2.7 Plasmon-enhanced photocatalysis

2.7.1. Surface plasmon resonance of the gold nanoparticles

Localized surface plasmon resonance (LSPR) is a unique characteristic of noble metals which is a result of the interaction of light with nanoparticles that are smaller than the wavelength of the light to excite the collective oscillations of the free electrons in the metal nanoparticles (Zhao et al., 2017, Petrayeyeva et al., 2011). **Figure 2.3** and **Figure 2.4** represent the interaction of light with a spherical (AuNS) noble metal and, gold nanorods (AuNRs) noble metal, respectively. The electric field results in the accumulation of electrons on one side and leaving the positive charge on the other side. Gold nanospheres have a characteristic deep red colour and one plasmon peak in the visible spectrum ranging from 510 nm to 550 nm (Das et al., 2011).

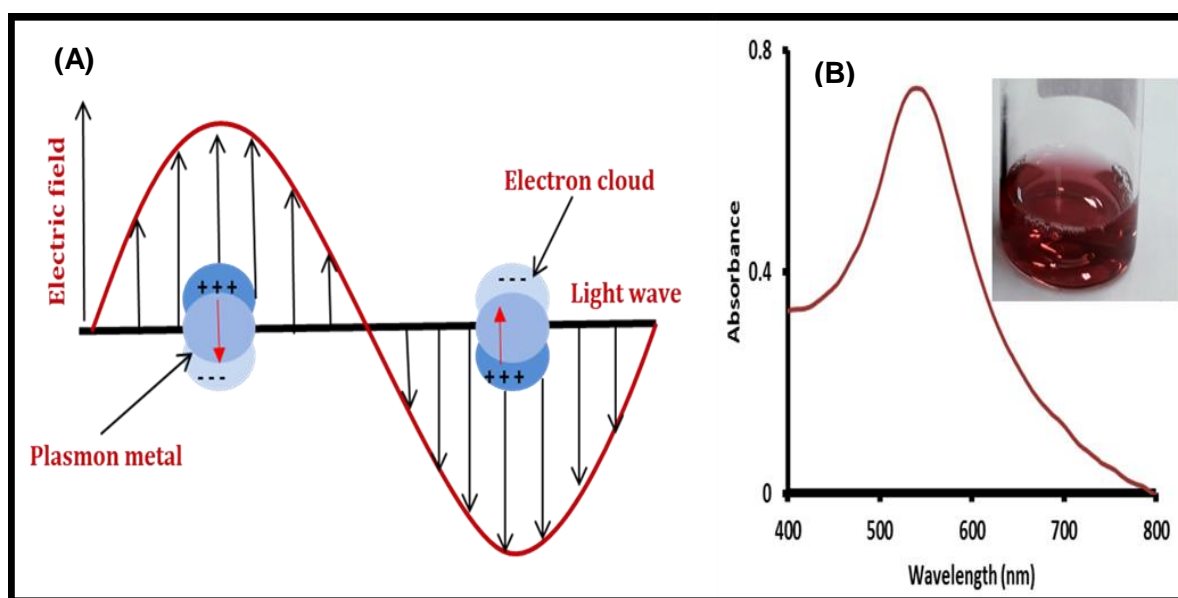


Figure 2.3: Schematic illustration of (A) AuNSs interaction with the electromagnetic field of visible light and (B) AuNS absorption plasmon band.

Unlike nanospheres, nanorods exhibit two characteristic plasmon peaks (transverse and longitudinal) in the visible spectrum to near infrared (NIR) (Shajari et al., 2017). The longitudinal peak of the nanorods can be tuned by changing the aspect ratio while the transverse peak remains stable. AuNRs are known to display a higher surface area compared to AuNS (Shajari et al., 2017).

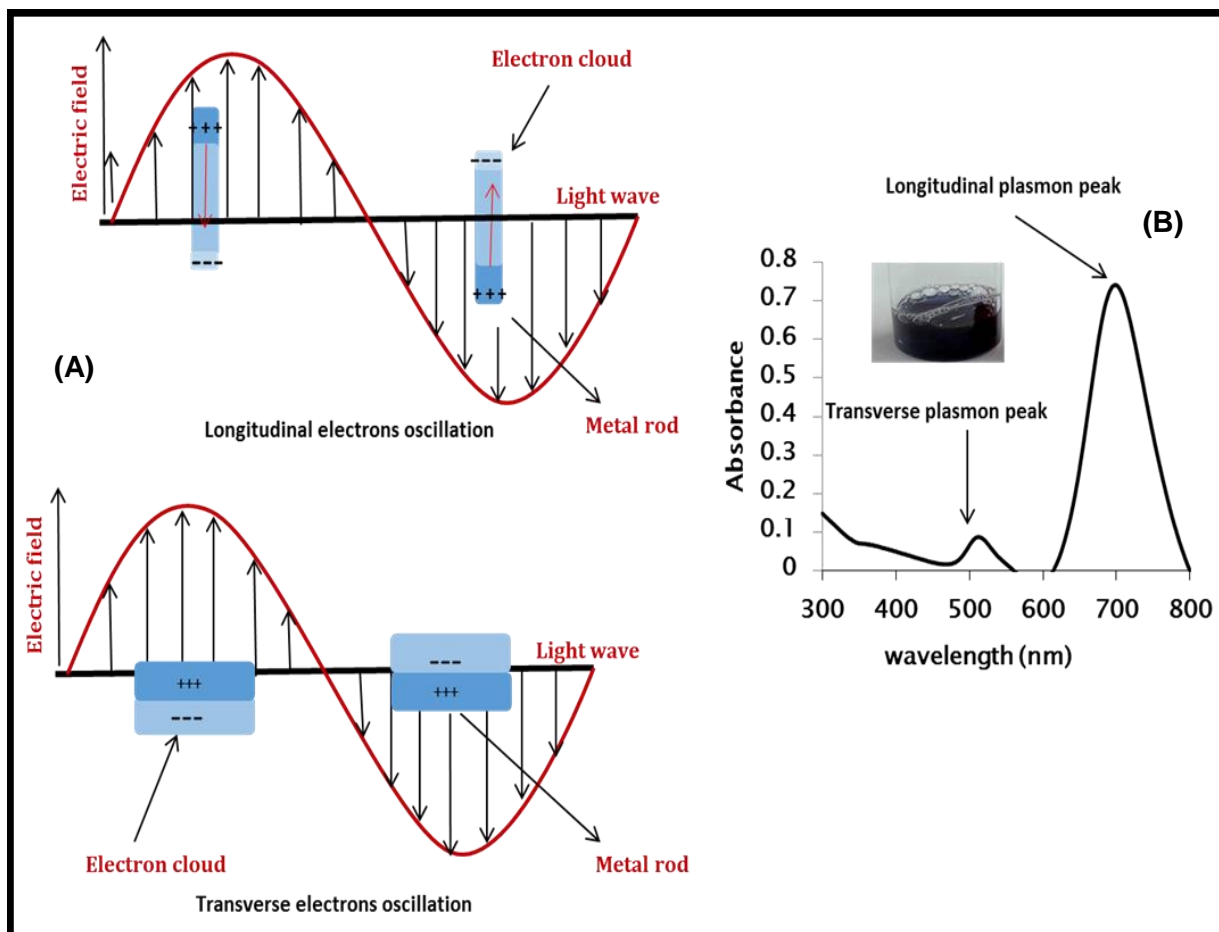


Figure 2.4: Schematic illustration of (A) AuNRs interaction with the electromagnetic field of visible light and (B) AuNRs absorption plasmon band.

2.7.2. Plasmon-enhanced mechanisms

Plasmon-assisted photocatalysis has recently been investigated in applications such as degradation of organics, reduction of carbon dioxide, and water splitting (Zhang et al., 2013). The enhanced photocatalytic efficiency in Plasmon metals semiconductor nanocomposites is attributed to the mechanisms described below: through Plasmon-enhanced mechanisms: (Zhang et al., 2017):

a) *Hot-electron injection mechanism*

This mechanism involves the transfer of charge carrier from the photo-excited metal to the conduction band of the semiconductor due to the formation of the Schottky barrier between the metal and the semiconductor (**Figure 2.5**). Generally, metals have lower Fermi levels than

semiconductors, therefore, when metals and semiconductors are in physical contact, from the equilibrium, the electron flow will be from the semiconductor to the metal (Arshad et al., 2017). The flow will continue until the Fermi level of the semiconductor reaches equilibrium with the Fermi level of the metals. This will lead to the deformation of the band structure between the semiconductor and the metal, which results in the formation of the Schottky barrier. The Schottky barrier serves as an effective trap for electrons and minimises the recombination effect.

b) Near field enhancement mechanism

Electromagnetic field-enhancement mechanism involves the interaction of the semiconductor with the intense surface plasmon resonance (SPR)-induced electromagnetic field in the surrounding of the plasmonic resonance nanostructure, which then results in the increase in rates of electron-hole pair formation in the semiconductor.

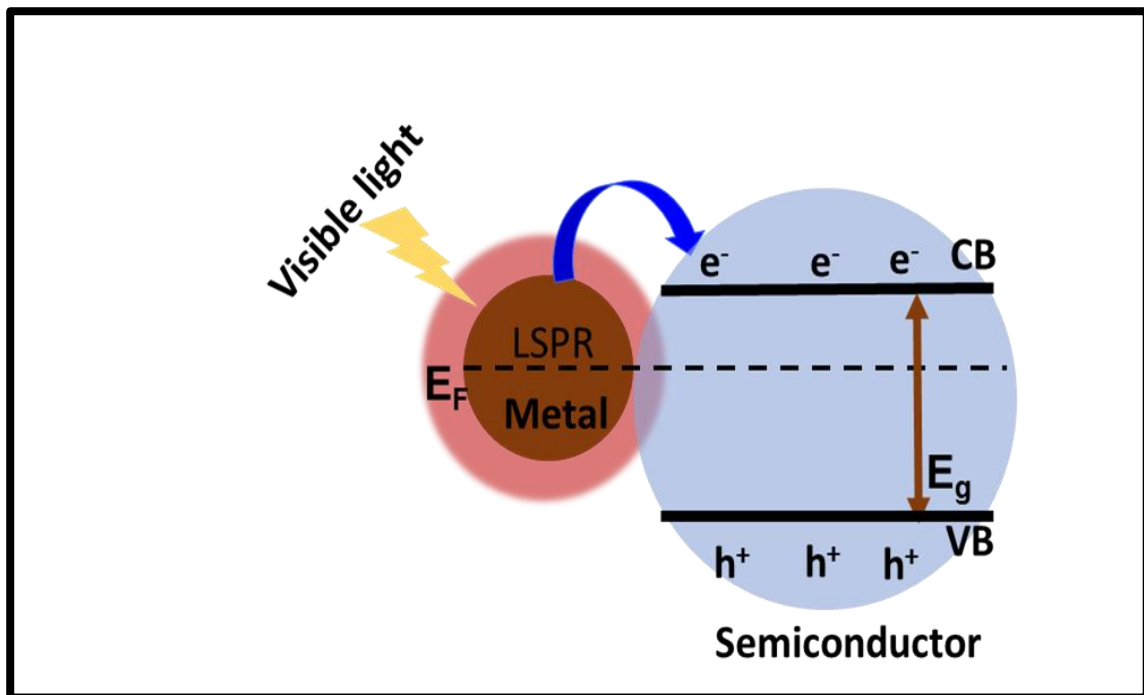


Figure 2.5: Schematic illustrations of charge transfer mechanism between plasmon metals and semiconductors under visible light.

2.8 Methods for synthesis for gold nanoparticles

Michael Faraday first discovered AuNPs in 1857 and since then a number of studies have been conducted (Thompson, 2007). The interest in AuNPs stems from their high stability, non-toxicity and strong absorption of visible to near-infrared light. (Tomar & Garg, 2013, Das et al., 2011). The shape of the gold nanoparticles is an important variable in controlling their chemical, optical and physical properties (Kumar et al., 2012). Thus, gold nanoparticles can be obtained in different shapes such as nanospheres (AuNS) (Kimling et al., 2006), nanorods (AuNRs), solution (Siti et al., 2013) nanocages (Chen et al., 2005), and nanoshells (Radloff et al., 2005). The synthesis of AuNPs using chemical methods is commonly used and consists of the reduction of gold by a chemical agent such as borohydrides, hydrazine and many others. The second part is the stabilization of Au-NPs using a capping agent such as a polymer, cetyltrimethylammonium bromide (CTAB) and others. The examples of these methods are discussed below.

2.8.1. Turkevich method

Turkevich first discovered the Turkevich method in 1951 (Turkevich et al., 1951) and it has become the most commonly used method. Typically an aqueous gold solution is heated to boil and finally a citrate agent is added to the boiling solution to reduce Au^{3+} to Au^0 . This method has been modified since it was designed by different researchers and yields only spherically shaped AuNPs.

2.8.2. Brust method

Brust and Schiffrin discovered this method in 1994 (Brust et al., 1994). In the first step, the gold chloroauric acid is transferred into toluene followed by the separation of the two phases by the addition of dodecanethiol, which reduces the Au^{3+} to Au^+ , thirdly sodium borohydride is added to the organic phase. The colour changes from orange to brown, which is an indication of the reduction of Au^+ to Au^0 and of the formation of AuNPs (Perala & Kumar, 2013).

2.8.3 Seed mediated method

The seed-mediated method is based on a two-step synthesis, i.e. the seed solution preparation step and the growth step. The seeds act as a nucleation site for the growth of AuNRs. The growth of the AuNRs continue in the presence of CTAB (capping agent) and ascorbic acid is used to slow down the reduction of the gold for good growth and yield (Das et al., 2011). The addition of AgNO_3 to the mixture is to control the yield of the formation of AuNRs (Das et al.,

2011). The size of the Au-NPs can be controlled by changing the ratio of the growth solution to the metal salt and the amount of AgNO₃ added to the solution (Siti et al., 2013).

2.9. Au/TiO₂ composites in photocatalysis

AuNPs processes have received significant attention in photocatalysis due to their ability to improve the efficacy in the removal of organic pollutants in the air and application in photocatalysis (Ayati et al., 2014). Different studies have reported on the photocatalytic performance of Au/TiO₂ nanocomposites (Bannat et al., 2009) **Table 2.3** shows examples of the literature studies that have been done on the degradation of organic dyes using Au/TiO₂ nanocomposites. It can be noted that most of these studies are only limited to spherically shaped nanoparticles. Furthermore, AuNRs remain to be explored thoroughly to understand the behaviour and the mechanisms involved.

Table 2.2: Summary of previous studies done on the degradation of organic dyes with Au/TiO₂

Catalyst	Pollutant	Morphology	light source	References
Au/TiO ₂	Methyl blue, methyl red and methyl orange	NSTs, NSs and NRs	visible	Kumar et al., 2017
Au/TiO ₂	Methylene blue	NSs	UV, Visible	Mesa, 2017
Au/TiO ₂	Patent blue V, dye.	NSs	UV	Vaiano et al., 2016
Au/TiO ₂ /SiO ₂	Methyl blue, Congo red and Rhodamine B	NSs	sunlight	Malik et al., 2016
Au/TiO ₂	Rhodamine B	NSs	UV	Alshammari et al., 2014
Au/TiO ₂	Methyl Orange	NSs	sunlight	Naik et al., 2013
Au/TiO ₂	Aafranin-O,SO, dye	NSs	UV	Bumajdad et al., 2013
Au/TiO ₂	Methyl Orange	NSs	sunlight	Padikkaparambil et al., 2013
Au/TiO ₂	Navy Blue	NSs	UV	Jagadale et al.,

Au/TiO ₂	Methyl Orange	NSs	UV, visible	Hou et al., 2011
Au/TiO ₂	Rhodamine B	NRs	UV	LU et al., 2011
Au/TiO ₂	Acid Orange 7	NTs	visible	Lou et al., 2011
Au/TiO ₂	Ethyl Orange, Organe II and Acid Red G	NSs	UV	Wang et al., 2008

2.10. Synthesis of Au/TiO₂ nanocomposites

There are several methods used for the preparation of Au/TiO₂ nanocomposites. Some of these are discussed below:

2.10.1 Impregnation and precipitation method

The impregnation method involves the distribution of metal precursors on the support surface; it is related to ion exchange or adsorption procedures, which interact with the surface of the supporting materials (Delannoy et al., 2006). Precipitation methods, on the other hand, can form the nanocomposite in the bulk solution. In the precipitation method the supporting materials act as nuclei for the crystallisation of the activation site precursor. Under the precipitation method, there is the coprecipitation method, which consists of mixing the support and the precursor together; the shape and size of the nanocomposites are obtained in one step (Prati & Villa, 2011).

2.10.2 Green synthesis method

This method involves the synthesis of AuNPs and metal oxides in different containers, each containing the plant extract. The solution of AuNPs is then slowly transferred into the metal oxide solution, followed by drying of the composite material at higher temperatures (Siti et al., 2013).

2.10.3 Self-assembly method

In a self-assembly method, the supported metal oxide with a high uniformity for metal elements is obtained. The pre-synthesised metal nanoparticles may be impregnated onto the metal-oxides support with an organic solvent. AuNPs is then added to the metal oxide solution; the obtained mixture is sonicated and left for ageing. The resulting Au/metal-oxide can be dried overnight at around 60 °C (Li & Zeng, 2006).

2.10.4 Hydrothermal method

Hydrothermal synthesis is a technique of crystallising materials at high temperature and pressure in aqueous solution. The technique depends on the solubility of the materials in a hot solvent at its critical point. Water has mostly been used a solvent in hydrothermal techniques. The procedure takes place in a sealed container called an autoclave. This method is good for the synthesis of large crystals without changing their composition and for the growth of high crystals with a high melting point at low temperature (Hayashi & Hakuta, 2010). Varying parameters such as temperature, pressure, pH and concentration during the synthesis can control the shape and size of the nanomaterials.

CHAPTER 3

MATERIALS AND METHODS

This chapter describes all the chemicals, equipment and methods used in this study for the synthesis and characterisation of the AuNPs and Au/TiO₂ and the degradation of reactive orange 16.

3.1. Materials

3.1.1. Reagents used for the synthesis of Au Nanoparticles and Au/TiO₂ nanocomposites

Gold(III) chloride trihydrate(99 %), gold standard solution (100 ppm), sodium borohydride (≥ 99.9 %), silver nitrate (≥ 99.9 %), trisodium citrate (99 %), Ascorbic acid (≥99.9 %), hexadecyltrimethylammonium bromide (≥ 98 %) , titanium butoxide (97 %), Ethyl-Diamine-Tetra-Acetic acid (≥ 98 %), Reactive orange 16 (≥ 70 %) were purchased from Sigma Aldrich. Methanol, ethanol and acetonitrile were purchased from Merck and were used as solvents in the apreparation of TiO₂ and the Au/TiO₂ composites. Ultrapure water with a resistivity of 18 Ω cm was used for aqueous solutions preparation (Milli-Q water).

3.2. Equipment

3.2.1. X-ray diffraction (XRD)

X-ray powder diffraction patterns were recorded on a BRUKER AXS D8 advance (X-ray diffractometer equipped with a LynxEye detector, using Cu-K α radiation ($\lambda_{K\alpha_1}=1.5406\text{\AA}$) tube. Data were collected in the range from 5° to 90° , scanning at 0.5 sec/step. X-ray diffraction scatters the atoms in the sample and if those atoms are arranged in order, then the scattered x-rays give the information of the atoms present in the sample and them arrangements in the material (Bunaciu et al., 2015). It is based on the principle of constructive and distractive interference of the monochromatic x-rays beam and the crystalline sample. When the sample interacts with the rays it creates constructive diffracted rays satisfying the Bragg's law, which is given the equation (Bunaciu et al., 2015):

$$n\lambda = 2d\sin\theta \tag{3.1}$$

Where n is an integer, λ the wavelength of the x-rays, d the interplanar spacing that generates diffraction and θ is the diffraction angle. The Bragg's law is the connection between the wavelength of the electromagnetic radiation to the diffraction angle and the lattice spacing in a crystalline sample. The diffraction peaks obtained to d -spacing permit to identify the element due to the fact that, each element as its own d spacing. The results obtained from the analysis are then comparing with the d -spacing of the standard reference patterns. The atomic planes of x-rays mapping are used for the identification phases and determination of structure in material science (Bunaciu et al., 2015).

3.2.2. Ultraviolet-Visible spectroscopy (UV-VIS)

The ground state electronic absorption spectra of the AuNPs and the composites were measured on a UV-1800 Shimadzu spectrophotometer. The degradation of reactive orange 16 was also monitored using this technique. The measurements were done by placing the liquid sample in a quartz cuvette, the reference cell contained the solvent (blank), the measurement was performed in the range of 200 nm to 800 nm. The instrument is equipped with light sources from tungsten and deuterium lamps. The relationship between the absorption of the sample and the concentration were done following the Beer-Lambert law, which is given by **Equation 3.2**:

$$A = \epsilon cl \tag{3.2}$$

Where A is the absorbance, ϵ the molar extinction, c is the concentration and l is the path length. In the visible region (400 nm to 800 nm), it is possible to predict the absorption wavelength of a substance from its colour. When the white light reflected by a coloured solution, a characteristic part of the mixed wavelength is absorbed, the rest of the light then absorbs the complementary to the wavelength that was absorbed (Kumar, 2006). **Figure 3.1** represents the wheel colour of the visible region.

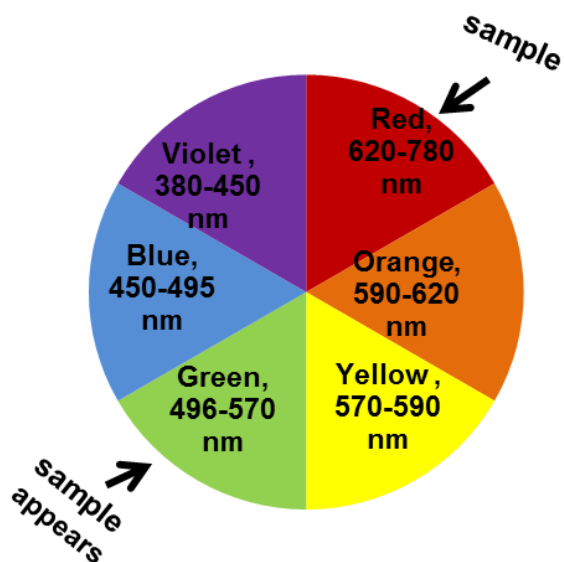


Figure 3. 1: Schematic illustration of the visible region wheel of colours.

3.2.3. Transmission electron microscopy

The transmission electron microscopy (TEM) images were obtained using a Tecnai TF20 thermionic transmission electron microscope at 100 kV accelerating voltage. TEM samples were prepared by placing a drop of sample on the sample grid and allowing it to dry before measurements. The sample measurement is done by a simple principle of using a beam of electrons that passes through an ultra-thin film of sample and it interacts with the sample while passing through. The electron beam obtained from the sample contains information about the structure of the sample (Kirkland et al., 2014).

3.2.4. Scanning electron microscopy

Scanning electron microscopy (SEM) images were obtained using 1450 scanning electron microscopy at the Electron Microscope Unit at the Western Cape University. The powder samples were coated using the K950X EMITECH sputter coater for 3 minutes before the analysis. The images provided are a result of the interaction of the electron beam with the atoms at different distances in the sample. The secondary electron is emitted and is detected by the electron detector, subsequently providing the 3D images (Stadtländer, 2007).

3.2.5. Fourier transform infrared spectroscopy

Infrared spectra were recorded on a Perkin Elmer 1000 series Fourier Transform Infrared (FTIR) spectrometer. The functional groups of the material can be easily identified by FTIR based its

unique absorption frequencies (Berthomieu & Hienerwadel, 2009). The vibrational energies are directly proportional to the absorption frequencies and the relationship is given by Hooke's law;

$$\bar{\nu} = \frac{1}{2\pi c} \sqrt{\frac{k}{\mu}} \quad (3.3)$$

Where $\bar{\nu}$, c , k , and μ is vibrational frequency, speed of light, force/spring constant and reduced mass of bonding atoms, respectively (Berthomieu & Hienerwadel, 2009).

3.2.6 Inductively Coupled Plasma—Optical Emission Spectroscopy (ICP-OES)

The concentration of gold atoms (Au^0) in AuNPs was determined using a Thermo Electron ICAP 6000 inductive coupled plasma with optical emission spectroscopy (OES) detector. Gold nanoparticles were digested by addition of 3 mL of aqua regia solution before the ICP Measurements (Gillespie et al., 2012). A standard calibration curve was achieved at concentrations ranging from 1 to 10 ppm. This technique was used for qualitative and quantitative analysis of trace-level element. The emission spectra of the samples were used for the identification of the element. When a sample is injected into the plasma, electrons are excited from the ground state to the excited state, the emitted energy is in photonic form, and the emitted photons have wavelength unique to their elements (Hou & Jones, 2000).

3.3. Synthesis of gold nanoparticles

Gold nanorods were synthesised according to using a seed-mediated method (Yang et al., 2013; Wu et al., 2016), and a modified Turkevich method was used for spherical gold nanoparticle (Tran et al. 2016).

3.3.1. Synthesis of gold nanorods

In a typical Au-NRs synthesis (**Figure 3.2**) the seed solution was prepared in the first step through reduction of 5 mL of 0.0005 M HAuCl_4 solution by 0.07 mL of 0.01 M sodium borohydride (NaBH_4) in the presence of 5 mL 0.234 M CTAB. The second step involved the preparation of a growth solution: 5 mL of 0.001 M HAuCl_4 was mixed with 5 mL of 0.234 M CTAB and 0.15 ml of 0.0045 M silver nitrate (AgNO_3) solution. 0.07 ml of 0.799 M ascorbic acid

(AA) was added to this mixture to achieve the reduction of Au^{3+} to Au^+ . 12 μL of the seed solution was added finally for complete reduction to Au^0 and the gold mixture was left to stand for 12 hrs to form the nanorods. The aspect ratio of the AuNRs was tuned by varying the amount of HAuCl_4 in the growth solution (Wu et al., 2016).

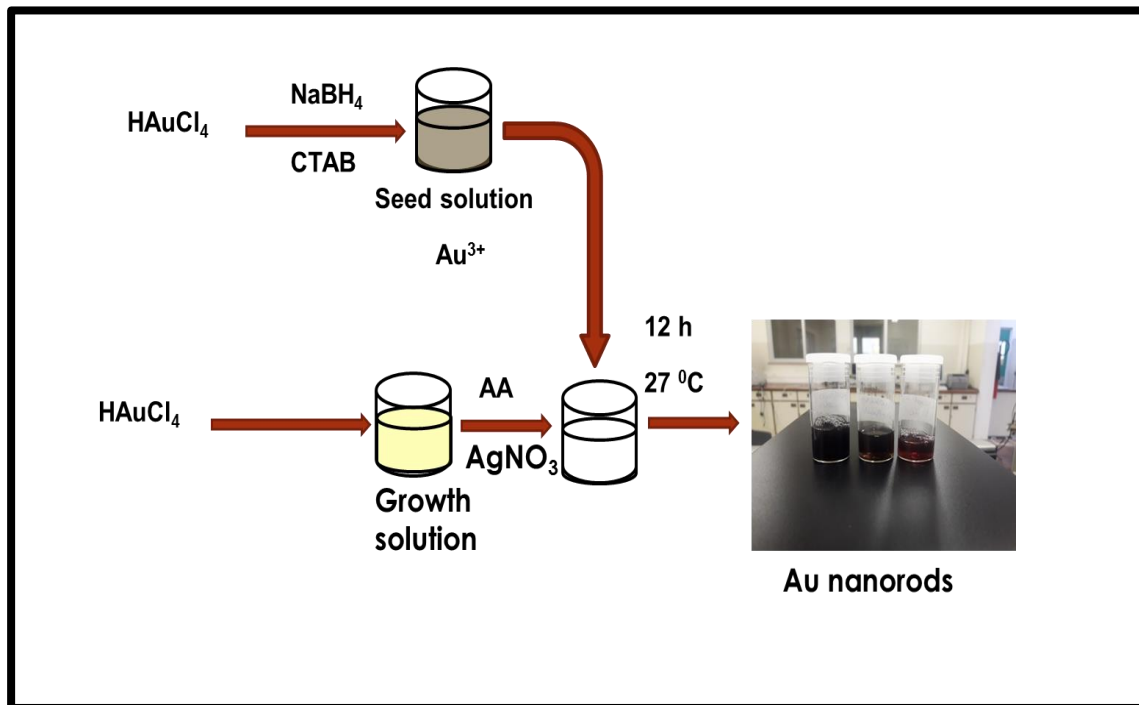


Figure 3. 2: Schematic illustration of seed-mediated method for the synthesis of Au nanorods (AuNRs).

3.3.2. Synthesis of gold nanospheres

AuNS were prepared according to a modified Turkevich method through the reduction of $\text{HAuCl}_4 \cdot 3\text{H}_2\text{O}$ solution with sodium citrate. Briefly, 36 mg of $\text{HAuCl}_4 \cdot 3\text{H}_2\text{O}$ was dissolved in 200 mL of distilled water under magnetic stirring. The solution mixture was heated to boil then 10 mL of a 1% sodium citrate was added rapidly. The deep-red colloidal solution of gold nanoparticles was obtained and then cooled to room temperature (Tran et al. 2016).

3.4. Synthesis of TiO_2 nanoparticles

Pure titanium dioxide nanoparticles were prepared using a sol-gel method. Firstly, titanium butoxide (titanium precursor) was dissolved in a methanol/ethanol mixture (50:50 v/v). The resultant titanium solution was stirred under reflux. Water was added into this mixture to perform

hydrolysis. The obtained sol was dried and finally calcined at 450 °C for 3 hours (Moon et al., 2018). **Figure 3.3** shows a schematic representation of the synthesis of TiO₂.

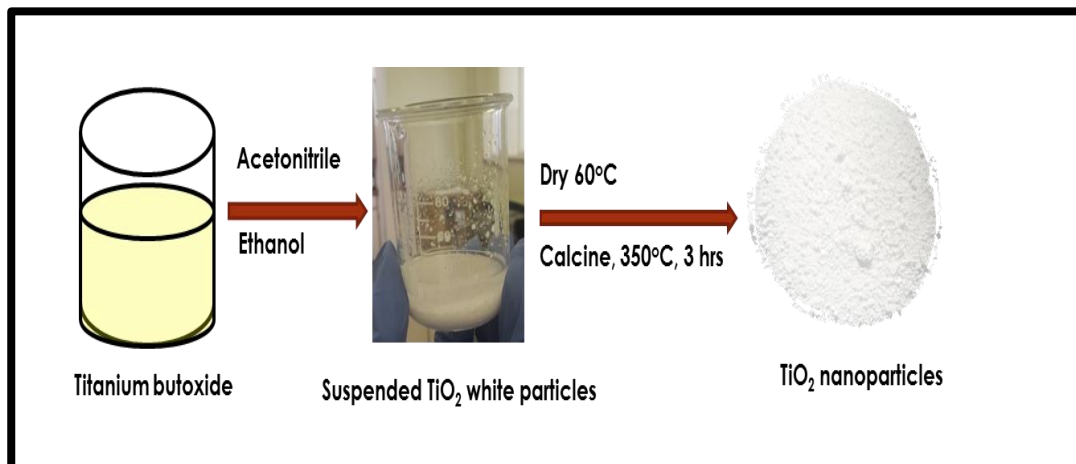


Figure 3.3: Schematic illustration of the synthesis of TiO₂ nanoparticles from titanium butoxide

3.5 Synthesis of Au/TiO₂ composites

Au/TiO₂ composites were synthesis by adding 8 mL (0.025 M) of CTAB aqueous solution into AuNPs (2 mL), and then 1.4 mL of EDTA-NH₃ (Li et al., 2014) was added into this mixture. Finally, 3 mL of Ti (OBU)₄ (97 %) solution drop wise and the reaction was stirred for 30 min at room temperature. This suspension was then dried at 90 °C for 5 hours. The reaction scheme for the synthesis of Au/TiO₂ composites is shown in **Figure 3.4**.

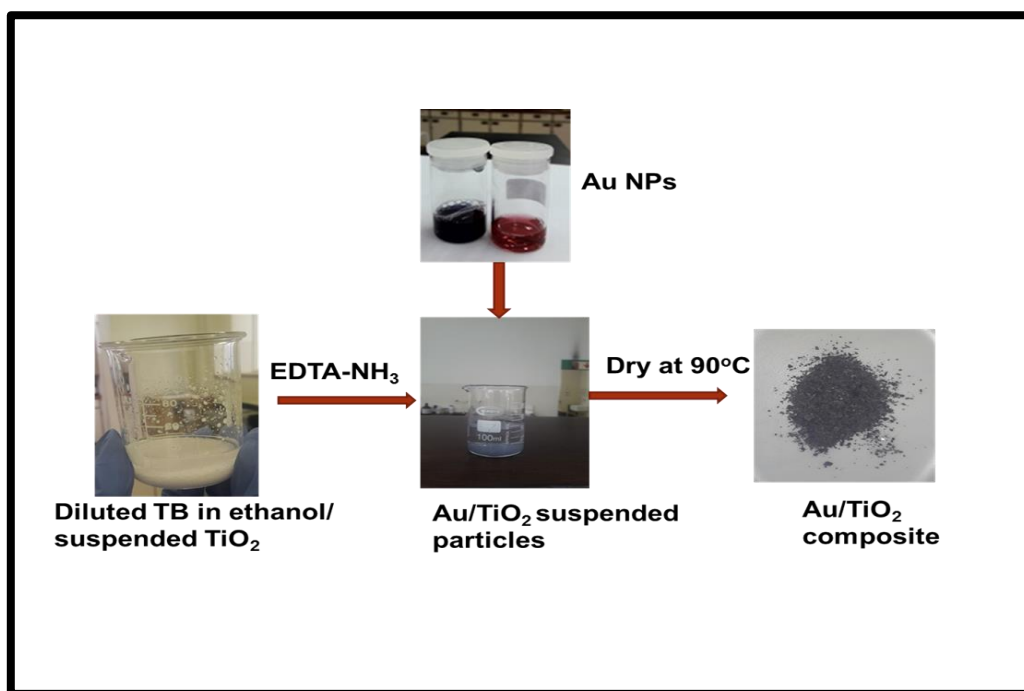


Figure 3.4. : Schematic illustration of the synthesis of Au/TiO₂.

3.6. Photocatalytic degradation of reactive orange 16

The photocatalytic activity of the AuNRs/TiO₂ composites was evaluated by the degradation of reactive orange 16 in aqueous solution under visible light. A 300 watts halogen lamp with a UV cut off filter was used to irradiate the samples. The photocatalyst was dispersed in a solution of reactive orange 16 at a 30 °C temperature in the presence of air. The suspension was stirred in the dark for 30 minutes to ensure an adsorption-desorption equilibrium between the dye molecules and the photocatalyst. **Figure 3.5** shows a typical set-up of photocatalytic testing. The degradation of reactive orange 16 was monitored by UV-VIS spectrophotometry after every 20 minutes.

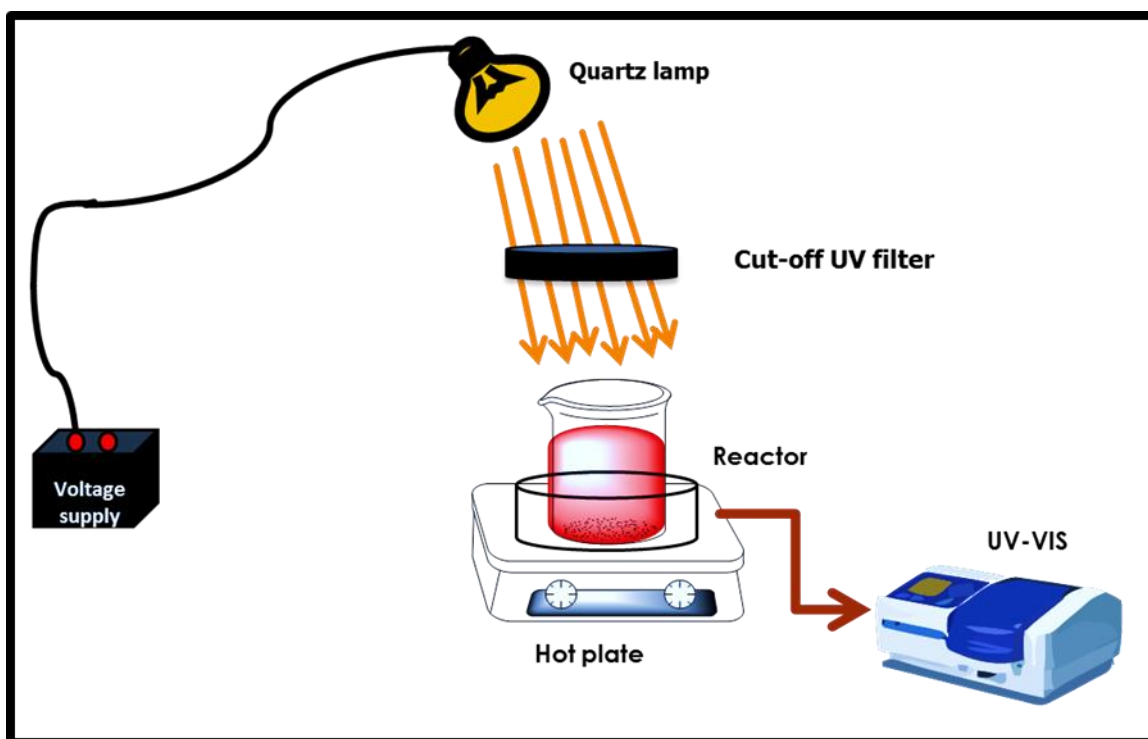


Figure 3.5. Schematic illustration of a typical set-up for testing of photocatalytic activity of Au/TiO₂ composites.

When the light irradiation was taking place, 4 mL of the solution was taken at an interval of 20 minutes. The samples collected were centrifuged to separate them from any catalyst particles in the solution and they were taken to the UV-Visible spectrophotometer for the monitoring of dye concentration. The percentage removal of the dye was calculated using **Equation 3.4**.

$$\text{removal (\%)} = 100 \times \frac{(C_0 - C)}{C_0} \quad (3.4)$$

Where C₀ and C are the concentrations of the dye at t=0 and t=t, respectively.

CHAPTER 4

CHARACTERISATION OF THE GOLD NANOPARTICLES AND Au/TiO₂ COMPOSITES

This chapter contains the discussion of the characterisation of the prepared Au and the Au/TiO₂ nanocomposites. The discussion includes the transmission electron microscopy (TEM) and scanning electron microscopy (SEM) for the analysis of the morphology and sizes. The discussion on the structural properties of the samples was done using the XRD and Fourier transformer infrared (FTIR) analysis. Furthermore, this chapter also contains the analysis of the properties of AuNPs for concentrations, molar extinctions and the number of particles per gold atom.

4.1. Quantification and properties of the gold nanoparticles

The concentration of Au in the synthesised AuNPs was quantified using ICP-OES. Three different AuNPs samples were synthesised and used in this work, gold nanospheres (AuNS), and gold nanorods with 1.9 and 3.4 aspect ratios (length/width). For the quantification of AuNRs, the particles were separated from the unreacted Au ions by the use of a centrifuge, the supernatant was discarded and the collected AuNRs were dispersed in 1 mL of milli-Q water. The obtained AuNRs were then digested with aqua regia for ICP-OES analysis. The quantification of AuNSs, 1 mL of this was also digested in aqua regia for ICP-OES analysis. The concentrations of the AuNRs obtained from the ICP-OES analysis were 10×10^{-5} M and 9×10^{-5} M for samples with 3.4 and 1.9 aspect ratios, respectively. AuNS were found to have the highest concentration of 10×10^{-4} M with a diameter of 28 nm as can be seen in **Table 4.1**. According to Orendorff & Murphy (2006), the amount of Au³⁺ reduced is independent of the aspect ratio of AuNPs but mostly depend on the initial concentration of Au³⁺ use in the synthesis. In the seed, the mediated method was used for the synthesis of AuNRs (**Section 3.3**), the growth solution was most important in the formation of the different aspect ratio of AuNRs. 5 mL of the growth solution was used to obtain AuNRs (3.4), meanwhile, 10 mL of the growth solution was used for AuNRs (1.9). The number of Au atoms per particle was calculated using **Equation 4.1** proposed by (Shang & Gao, 2014). A perfect sphere and cylinder were assumed for AuNS and AuNRs, respectively. The calculation was also based on the assumption of a complete reduction of the Au³⁺ to form nanoparticles. **Equations 4.1, 4.2 and 4.3** were used to calculate the number of gold particles for spherical particles, the number of gold particles for rod-shaped particles and the extinction coefficient, respectively (Shang & Gao, 2014).

$$N_{\text{AuNRs particles}} = \frac{V\rho}{M} N_A \quad (4.1)$$

$$N_{\text{AuNS Particle}} = \frac{\rho\pi d^3}{6M} N_A \quad (4.2)$$

$$\varepsilon = Ad^\gamma \quad (4.3)$$

Where M is the molar mass of gold (g/mol), ρ is gold density (g/nm³), d is the diameter of gold nanoparticles (nm) and N_A is the Avogadro constant, $A = 4.7 \times 10^4 M^{-1} \text{cm}^{-1}$, $\gamma = 3.30$ for nanoparticles with diameter $d \leq 85 \text{ nm}$.

Table 4. 1 Concentration, extinction coefficients, wavelength and the number of particles per atoms of gold nanorods and spheres.

AuNPs (nm)	[Au] (M)	λ_1 (nm)	λ_2 (nm)	ϵ_1 (M ⁻¹ cm ⁻¹)	ϵ_2 (M ⁻¹ cm ⁻¹)	Np
AuNRs (3.4*)	7×10^{-5}	514	701	1.07×10^6	6.69×10^7	2.7×10^3
AuNRS (1.9*)	9×10^{-5}	527	643	6.35×10^7	5.01×10^8	5.7×10^4
AuNS (28)	10×10^{-4}	537	NA	3.09×10^9	NA	7.4×10^5

(*aspect ratio)

The extinction coefficient of gold nanorods increased as the aspect ratio decreased from 3.4 to 1.9 (**Table 4.1**). The number of gold particles was found to decrease in the following order: AuNRs (3.4) > AuNRs (1.9) > AuNS (28) (**Table 4.2**). The calculations of these values were done according to the sizes obtained from the TEM. The extinction coefficient of gold nanospheres was found to be $3.06 \times 10^9 \text{ M}^{-1} \text{cm}^{-1}$ for gold with a diameter of 28 nm.

4.2. Microscopic analysis of Au and Au/TiO₂ nanocomposites

Three different AuNPs samples were synthesised: gold nanospheres (AuNS) and two gold nanorods samples with a difference in aspect ratio (length/width). The three AuNPs were used in the synthesis of Au/TiO₂ photocatalyst. **Figure 4.2** shows the morphology of the gold nanoparticles with their corresponding Au/TiO₂ nanocomposite. The particles sizes of the synthesised AuNPs were measured using ImageJ 6 software and these particles sizes were

used in the calculation of molar extinction and the number of Au nanoparticles. **Figure 4.1 (A)** shows TEM images of gold nanospheres with an average diameter of 28 nm. The calculated aspect ratios (L/W) of the gold nanorods in **Figure 4.1 (B) and (C)** were 1.9 nm ($L= 16.62$, $W=8.72$) and 3.4 nm ($L=9.23$, $W=2.68$). The different aspect ratios of AuNRs were obtained by varying the volume of the growth solution added to the final mixture solution. The TEM images of the corresponding composites show gold nanospheres and nanorods embedded in the TiO_2 , which confirms the formation of the composite photocatalysts.

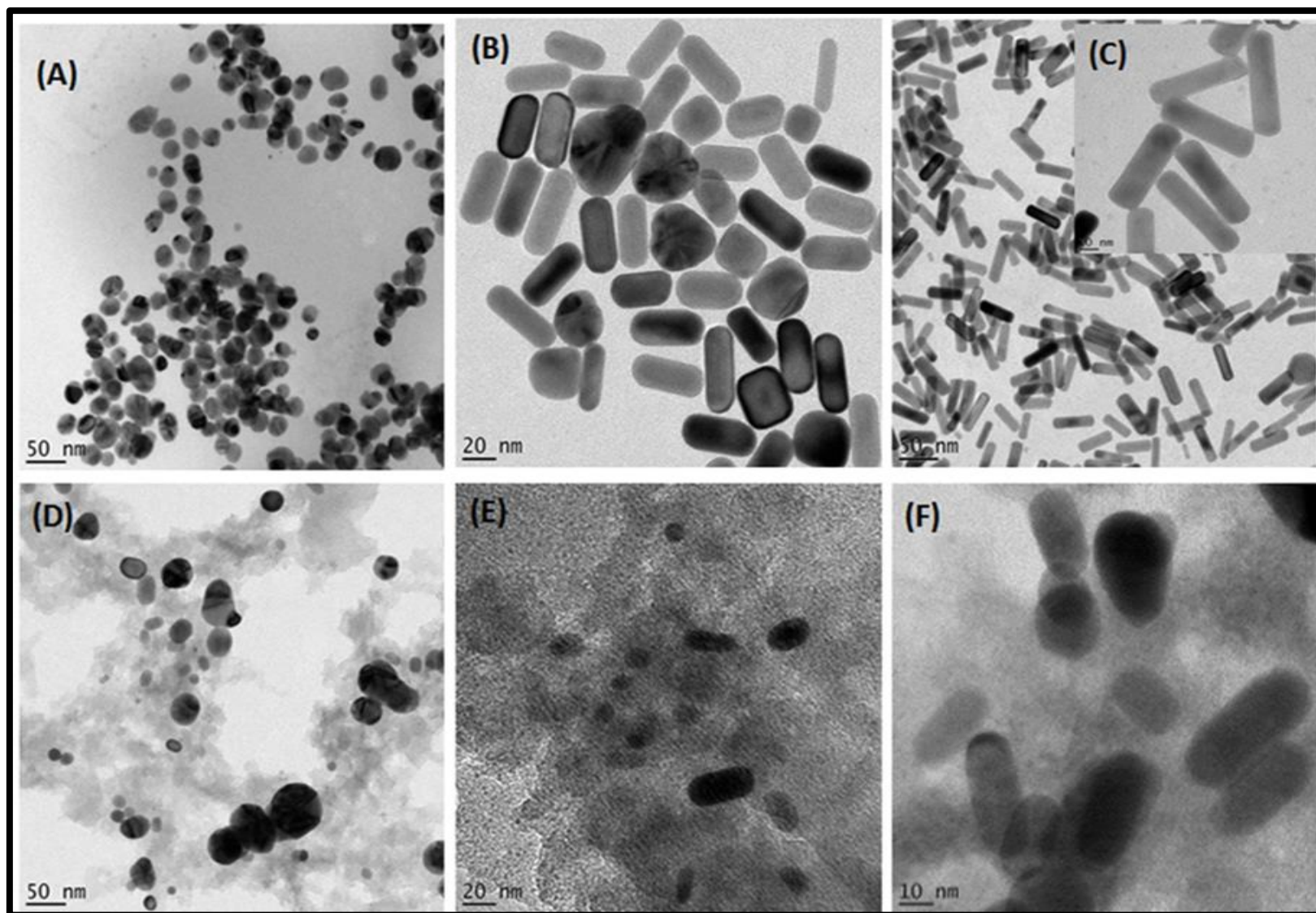


Figure 4.1: TEM images (A) AuNS, (B) Au (1.9) NRS, (C) Au (3.4) NRs, (D) AuNS/TiO₂, (E) AuNRs (1.9)/ TiO₂ and (F) AuNRS (3.4)/TiO₂.

The SEM images in **Figure 4.2 (A, B, C and D)** show the distribution and the morphology of the Au/TiO₂ composites. AuNPs show a good dispersion on the surface of TiO₂ and this was also confirmed by EDS which reveal the presence of Au, Ti, O, and elements as expected in the Au/TiO₂ composites.

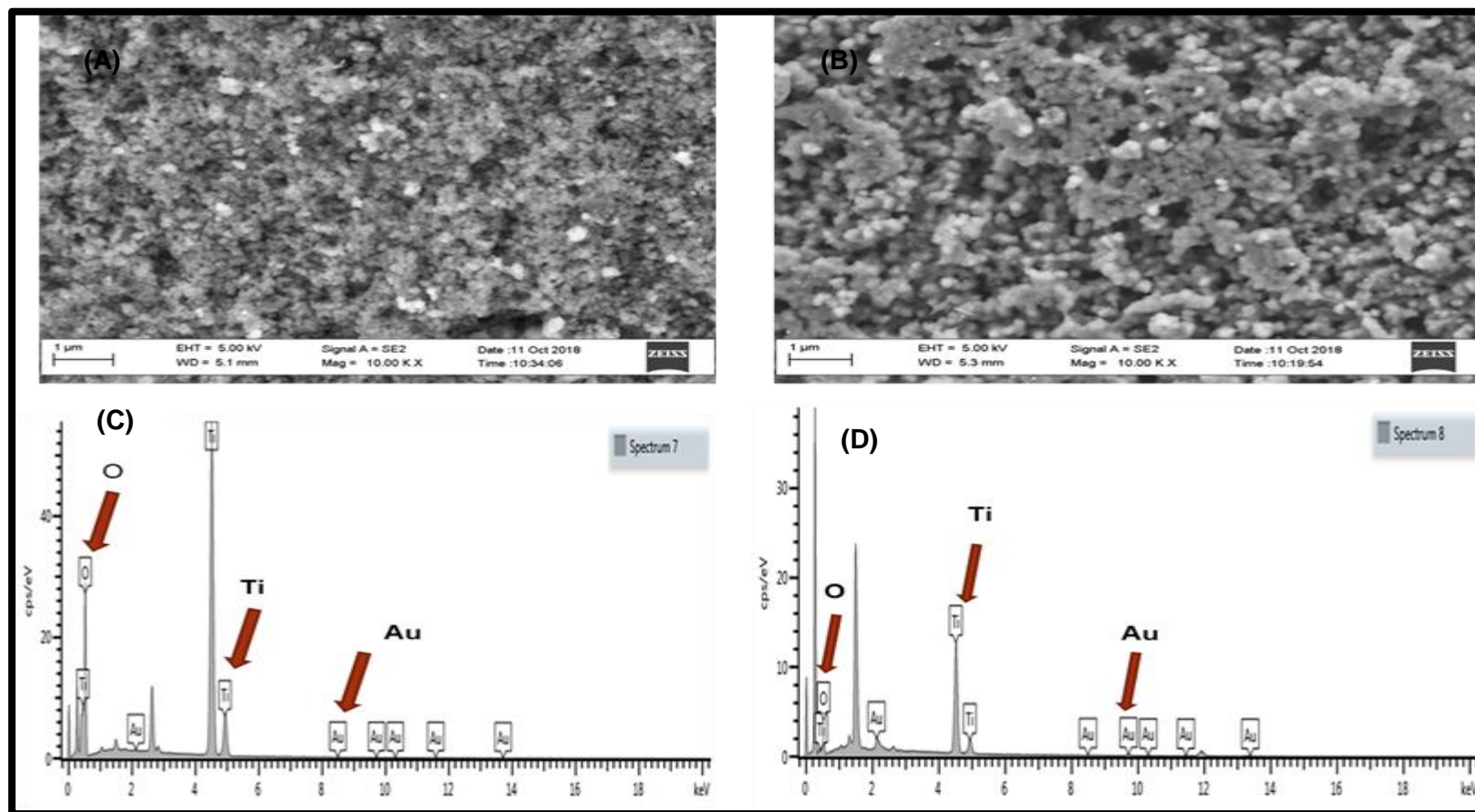


Figure 4.2: SEM images of (A) AuNS/TiO₂, (B) AuNRs/TiO₂, (C) and (D) their corresponding EDS.

4.3. Optical properties of Au nanoparticles, TiO₂ and Au/TiO₂ nanocomposites

The optical absorption properties of AuNPs and their corresponding composites were analysed using a UV-Vis spectrophotometer. **Figure 4.3 (A)** shows the UV-Vis spectrum of the AuNS and AuNRs, with one plasmon peak, at 537 nm for AuNS. AuNRs (1.9) showed the two distinct plasmon peaks at 643 nm and 527 nm and AuNRs (3.4) at 701 nm and 514 nm. The presence of the two peaks in the visible spectrum is the foremost characteristic of the AuNRs. The transverse peak is a result of the oscillations across the width, while the longitudinal peak is the oscillations along the length of the nanorods. The second plasmon peak (longitudinal) is dependent on the aspect ratio of the AuNRs, whereas the transverse peak is not affected by changes in aspect ratio.

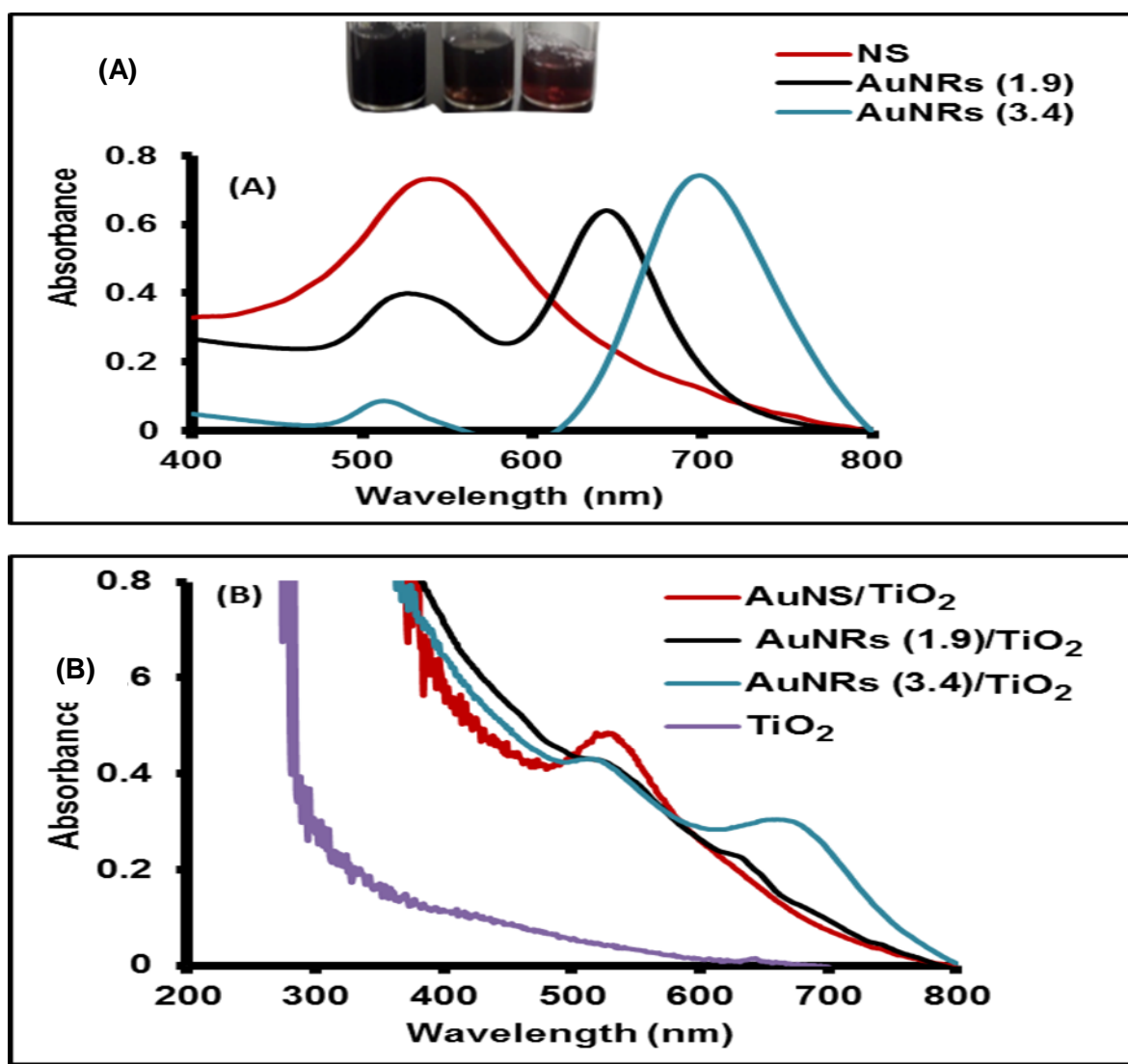


Figure 4.3: UV-Visible spectra (A) of AuNS, Au nanorods (1.9), gold nanorods (3.4) and (B) AuNS/TiO₂, AuNRs (1.9)/TiO₂, AuNRs(3.4)/TiO₂ and TiO₂.

The UV-Vis absorption spectra of TiO₂ and Au/TiO₂ nanocomposites are shown in **Figure 4.3 (B)**. The UV-Vis spectrum of the TiO₂ nanoparticles shows a peak at 373 nm, corresponding to the band gap of 3.3 eV as calculated by **Equation 4.1**.

$$E_g = \frac{1243}{\lambda} \quad (4.1)$$

Where E_g is the band gap and λ is the wavelength. The Au/TiO₂ nanocomposites show the plasmon peaks in the visible region due to the presence of AuNPs. The formation of the Au/TiO₂ nanocomposites results in a Schottky barrier (SB) at the interface between Au and TiO₂. The schottky barrier height (SBH) is considered as one of the important factor, which influences the plasmon-induced electron injection at Au/TiO₂ interfaces (Arshad et al., 2017). The SBH of 0.8 eV in Au/TiO₂ was calculated using **Equation 4.2** (Arshad et al., 2017).

$$\phi_{SB} = \phi_M - X \quad (4.2)$$

Where ϕ_{SB} is the Schottky barrier height, ϕ_M is the metal work function and, x is the semiconductor electron affinity. The values of Au work function and electron affinity for TiO₂ are 5.1 eV and 4.3 eV, respectively (Hossein-Babaei et al., 2015, Arshad et al., 2017). The higher the Schottky barrier height, the higher the ability of the metal to trap electrons, and preventing them from falling back to TiO₂. Au has a higher work function compared to TiO₂. Due to this difference in work function the electron transfer will be from TiO₂ to the Au interface for the equilibration of the Fermi level, and that results in the reduction of the work function of Au/TiO₂ nanocomposites. The reduction of the work function of Au/TiO₂ means that more charge migration at the interface of the catalyst (Khoa et al., 2014).

4.4. Structural properties of Au nanoparticles, TiO₂ and Au/TiO₂ nanocomposites

The x-ray diffraction patterns of the synthesised TiO₂ and Au/TiO₂ nanocomposites are shown in **Figure 4.4**. The distinctive peaks at 2θ angles demonstrate the (101), (004), (200), (211), (204), (220), (215), (224) crystal planes. The XRD patterns were indexed to the TiO₂ anatase phase according to the ICDD database. This was also confirmed by the presence of the strong (101) peak at 25° (2θ) in TiO₂ and Au/TiO₂ nanocomposite (Thamaphat et al., 2008). The observed (111) and (200) crystal planes were indexed to gold nanoparticles in the composite samples. The broadness of the peaks indicates the crystalline nature of the TiO₂ and the composites. The

interplanar spacing was calculated using **Equation 3.1** (Bunaciu et al., 2015). The values of d are given in **Table 4.2** below.

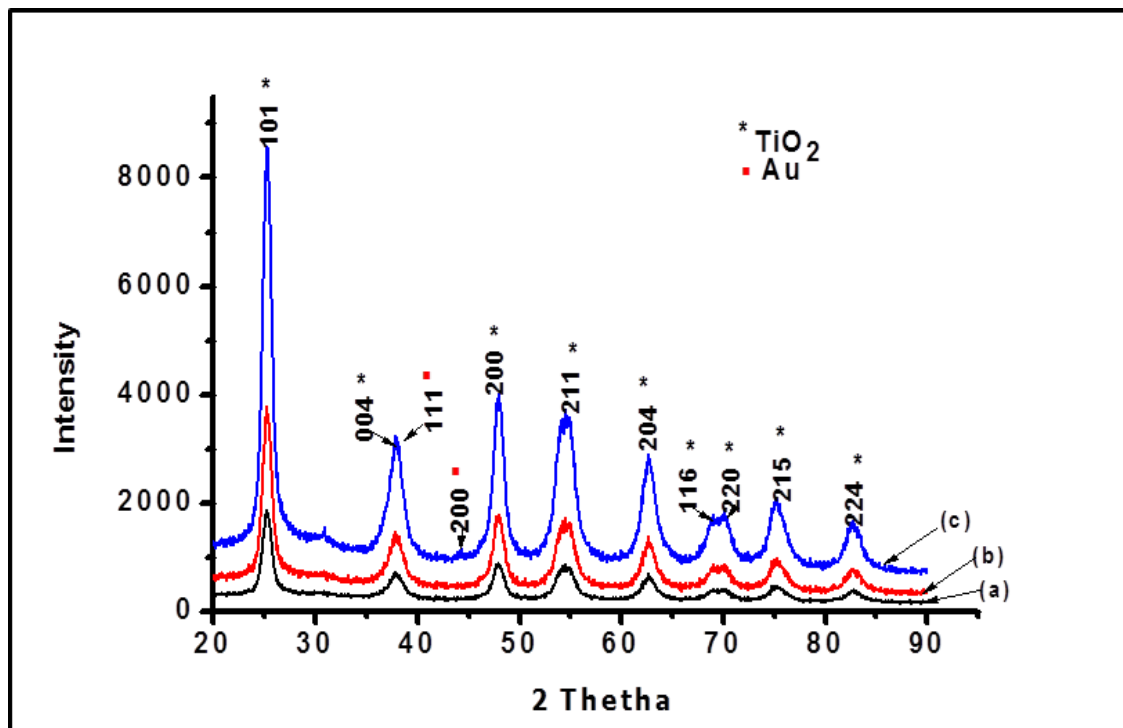


Figure 4.4: XRD patterns of (A) TiO₂ and (B) AuNRs/TiO₂ nanocomposites and (C) AuNS/TiO₂.

Table 4. 2 XRD data of Au/TiO₂ nanocomposites

2θ	θ	Sinθ	λ(nm)	n	d-spacing (nm)
25	12.5	0.2164	0.154	1	0.0167
38	19	0.3255	0.154	1	0.0251
45	22.5	0.3826	0.154	1	0.0295
48	24	0.4067	0.154	1	0.0313
55	27.5	0.4617	0.154	1	0.0356
64	32	0.5299	0.154	1	0.0408
70	35	0.5735	0.154	1	0.0442
75	37.5	0.6087	0.154	1	0.0469
83	41.5	0.6626	0.154	1	0.0510

The Fourier transform infrared (FTIR) spectrum in **Figure 4.5** shows a broad band at 3350 cm^{-1} , corresponding to the hydroxyl stretching (OH) of TiO_2 . The peak at 1632 cm^{-1} is the bending mode of water (H-O-H, Ti-O-H). The Ti-O stretch was observed at 1395 cm^{-1} and 1383 cm^{-1} (León et al., 2017). Meanwhile, the C-H stretching mode of the aliphatic carbonyl group was attributed to the vibrations at 2916 cm^{-1} , 2848 cm^{-1} and 2972 cm^{-1} . The C-O broad stretch was observed at 1245 cm^{-1} . The presence of C-O and C-H may be due to the titanium butoxide used in the synthesis of the conjugates. Furthermore, The presence of the titanium butoxide residues in the conjugate can be attributed to the low temperatures used for the synthesis which was not efficient to degrade all the organic residues. The use of low temperatures is due to the fact that gold nanorods tend to lose their rod shape at high temperatures during calcination (Gołabiewska et al., 2016). The peaks below 700 cm^{-1} indicate the metal oxide vibrational modes (Ti-O-Au, Au-O and Ti-O) (Kumar et al., 2016) due to the formation of the composite between the AuNPs and TiO_2 .

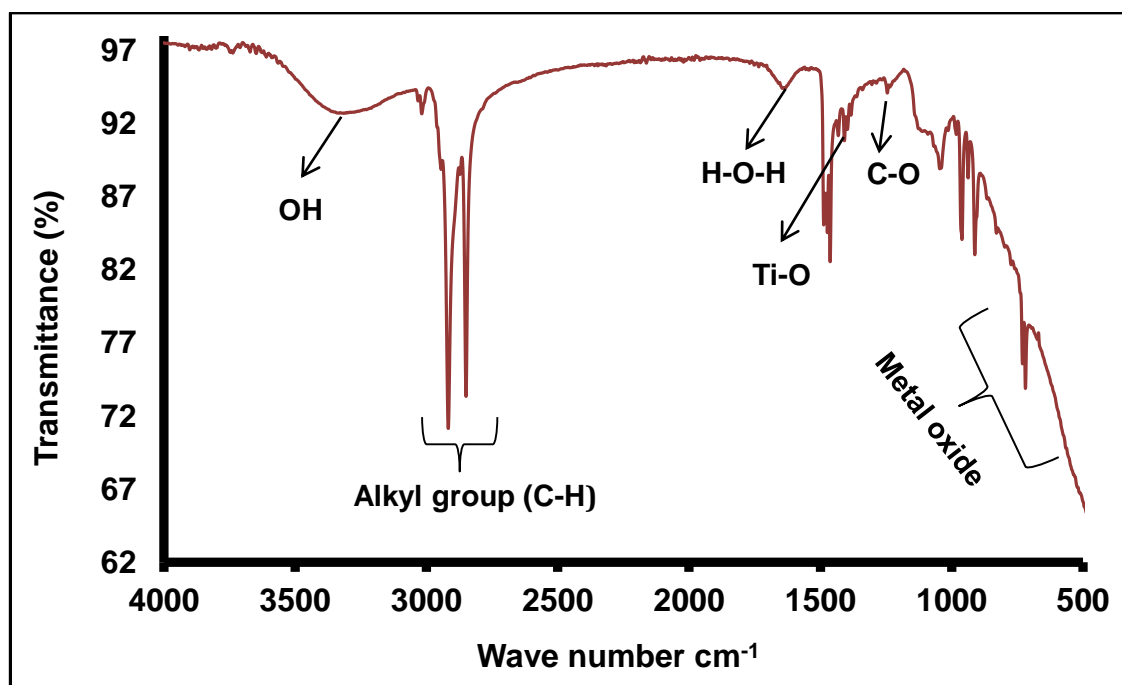


Figure 4.5: Fourier Transform Infrared (FTIR) spectrum of Au/TiO₂ nanocomposites.

In summary, the characterization results clearly showed that Au/TiO₂ nanocomposites were successfully obtained. The shape and the size of the AuNPs and the composites were defined from the TEM analysis. The UV-Vis analysis also proved the formation of nanocomposite materials.

CHAPTER 5

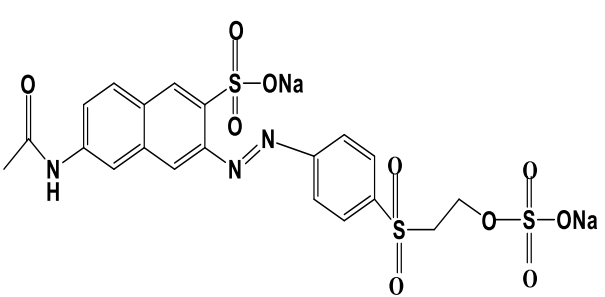
PHOTOCATALYTIC DEGRADATION OF REACTIVE ORANGE 16

This chapter presents the results of the effect of shape and size of the AuNPs on the photocatalytic degradation of reactive orange dye as a model azo dye. In order to evaluate the effect of the size of the gold nanoparticles on the plasmonic photocatalytic performance, the three photocatalysts were compared and presented herein. Three different photocatalysts were prepared by loading AuNS, and AuNRs with different aspect ratios (1.9 and 3.4). The three photocatalysts are denoted as AuNS/TiO₂, AuNRs (1.9)/TiO₂ and AuNRs (3.4)/TiO₂. The effect of a mixed shapes (nanospheres and nanorods) was also investigated and for their synergetic effects on the photocatalytic activity.

5.1. Properties of reactive orange 16 (RO 16) dye

Reactive orange 16 belongs to the class of reactive dyes and its structure consists of two sulfonate groups. RO 16 is commonly used for dyeing cotton in the textile industry (Anouar et al., 2014). The general characteristics of RO 16 are summarized in **Table 5.1**. RO 16 was used as a model dye in this study.

Table 5.1: Characteristic data of reactive orange 16

Dye structure	Properties
 <p>The chemical structure of Reactive Orange 16 is shown. It consists of a naphthalene ring system. At the 6-position of the naphthalene ring, there is a sulfonate group (-SO₃Na). At the 2-position, there is a hydrazinylidene group (-N=N-) attached to a benzene ring. This benzene ring has a sulfonate group (-SO₃Na) at the 4-position and a sulfonate group (-SO₃Na) at the 2-position, which is connected to a propyl chain (-CH₂-CH₂-CH₂-) that is also attached to a sulfonate group (-SO₃Na).</p>	<ul style="list-style-type: none">➤ IUPAC Name: Disodium (3Z)-6-acetamido-4-oxo-3-[[4-(2-sulfonatooxyethylsulfonyl)phenyl]hydrazinylidene] naphthalene-2-sulfonate➤ Wavelength: 388 nm, 494 nm➤ Dye class: azo dye➤ Mw: 617.54➤ Molecular formula: C₂₀H₁₇N₃Na₂O₁₁S₃

5.1. Shape and size effect on the photodegradation and decolourization of RO 16.

The optical properties of AuNPs are influenced by changes in shape and size and in turn, affect surface plasmon resonance (SPR) parameters. In comparison to AuNS with one plasmon peak, AuNRs possess two distinct plasmon peaks and both the longitudinal and transverse peaks may participate in the enhancement of the photocatalytic activity (Liu et al., 2013). The longitudinal plasmon band can be tuned by varying the aspect ratio of AuNRs across a wide spectral range, from the visible spectrum to the near-infrared spectrum (Chen et al., 2013). The photocatalytic activity depends not only on the plasmon metal shape but also on their size. Recently, the effect of size of the AuNPs (AuNS) on the photocatalytic activity of TiO₂ has been investigated (Kumar et al., 2017, Gołębiewska et al., 2016). However, the comparison between the photocatalytic effect of short and long AuNRs have been overlooked. In this study, the photocatalytic activity of TiO₂ containing AuNRs with different aspect ratios (1.9 and 3.4) was investigated. The photocatalytic performance of the photocatalyst containing AuNRs was also compared with the one loaded with AuNS. **Figure 5.1 (A, B and C)** below presents the change in concentration of the photodegradation of RO 16 for the three different AuNRs(3.4)/TiO₂, AuNRs(1.9)/TiO₂, and AuNS/TiO₂, respectively. The shift in the absorption band of the characteristic peak of RO 16 was observed (**Figure 5.1**) during the photocatalytic process which was due to the interaction of the dye molecules with the photocatalyst.

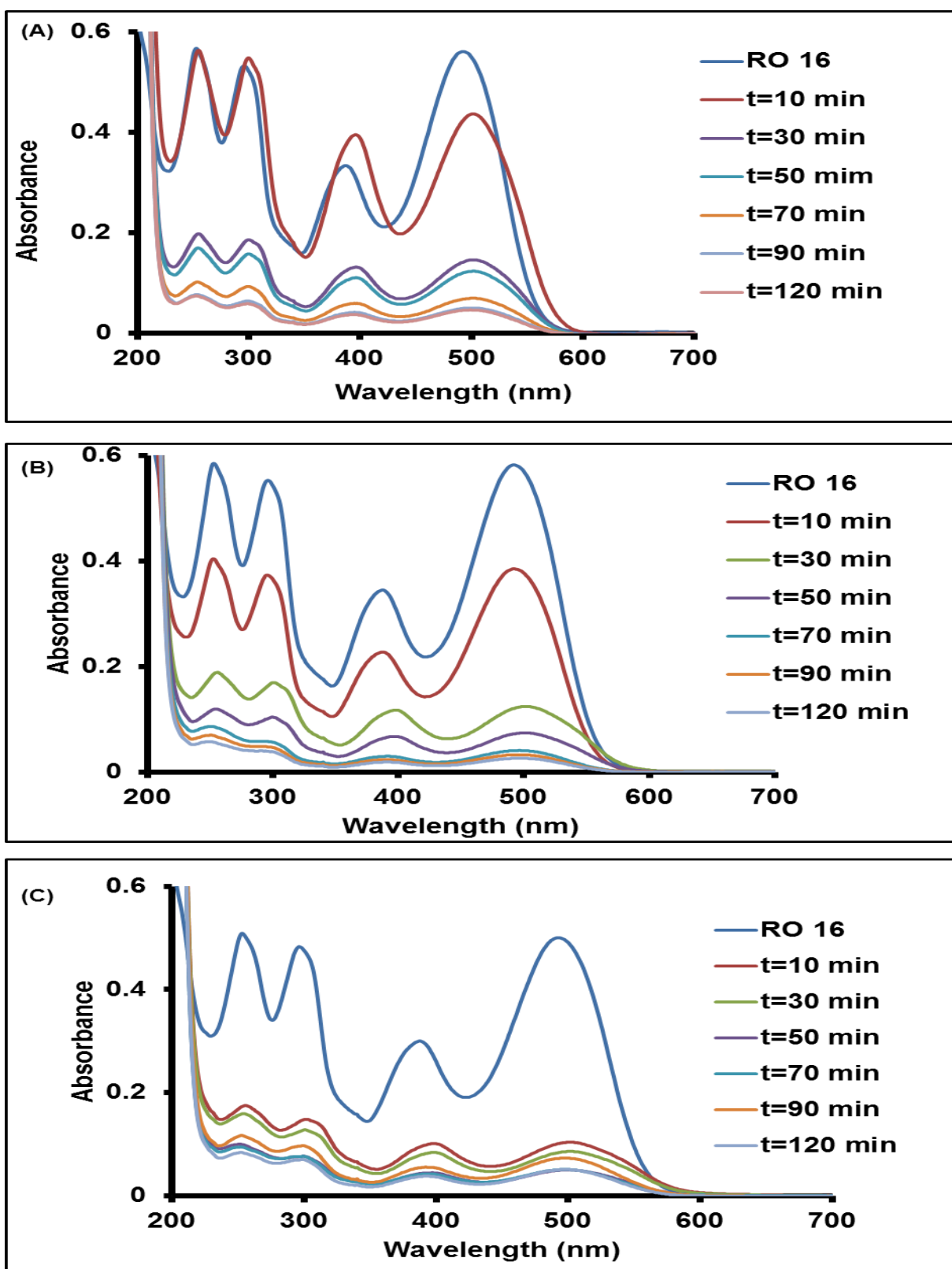


Figure 5.1: Absorption spectra of the change in concentration of RO 16 [C=20 ppm, C_{cat}= 0.2 g/L, pH= 6.7] using AuNRs(3.4)/TiO₂ (A), AuNRs(1.9)/TiO₂ (B). And AuNS/TiO₂ (C) as catalysts.

The stability of RO 16 was monitored by exposing the dye solution to light without any photocatalyst. However, as can be seen in **Figure 5.2**, the dye was not degraded in the absence of a photocatalyst. This shows that the photocatalyst was responsible for the decolourization of the dye under visible light. The photoactivity of the TiO_2 alone (without AuNPs) was also investigated under visible light and it was observed that TiO_2 alone did not show any photoresponse under visible light due to its inability to absorb visible light. Therefore, it can be said that the visible light photodegradation of RO 16 was induced by the presence of gold nanoparticles through plasmon enhanced mechanisms.

Figure 5.2 shows a higher photocatalytic efficiency for the AuNRs compared to AuNS. The degradation efficiencies were 86.65 % and 84.56 % for AuNRs with an aspect ratio of 3.4 and 1.9, respectively, and 79.24 % for AuNS. This can be explained by the fact that for the AuNRs both the transverse and the longitudinal peaks participate in the photocatalytic process which results in significant enhancement of the electromagnetic field (Liu et al., 2013). The enhancement of the electromagnetic field results in the generation of intense hot spots which increases the rate of the electron/hole formation. Previous studies based on the effect of the shape of the AuNPs have had also reported that the geometry of the AuNPs has a considerable effect on the photocatalytic performance (Gołębiewska et al., 2016, Kaur & Pal, 2012). Gołębiewska et al. (2016) reported a higher photocatalytic activity for AuNS compared to AuNRs. In this study, the transverse plasmon peak was directly excited and not the longitudinal peak. The effect of AuNRs aspect ratio shows that the shorter the AuNRs length the higher the photocatalytic activity, AuNRs with an aspect ratio of 3.4 (length 9.23 nm and width 2.68 nm), showed the higher photocatalytic performance compare to AuNRs with an aspect ratio of 1.9 (length 16.6 nm and width 8.72 nm). A similar study was done by Tanabe et al. (2015) where they reported that the photocatalytic effects were independent of the AuNRs aspect ratio when the width is the same. However, in this study, AuNRs samples had different widths and length which can explain the differences in their photocatalytic performances.

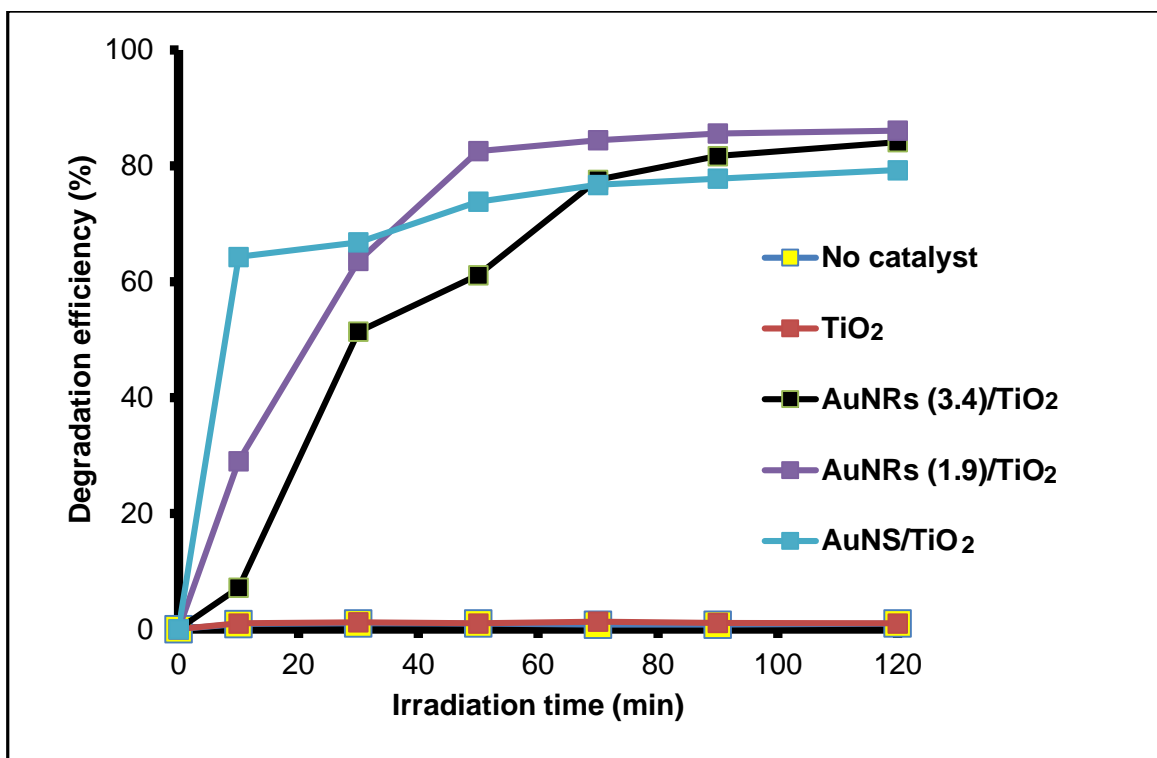


Figure 5.2; Degradation efficiency of RO 16 [C=20 ppm, C_{cat}= 0.2 g/L, pH= 6.7] AuNRs (3.4)/TiO₂, AuNRs (1.9)/TiO₂, AuNS/TiO₂, no catalyst and TiO₂.

5.3. Kinetics of the photodegradation of RO 16

During the photocatalytic process, the concentration of RO 16 was changing as a function of time. As expected the shape and size of AuNPs had a significant impact on the photodegradation rate of RO 16. The change in rate was a confirmation of the formation of the more active site on TiO₂ on the kinetics process. The Langmuir-Hinshelwood kinetic model is the most used for the photodegradation process of azo dyes (Flores et al., 2014) with the rate given by **Equation 5.1** below.

$$rate = \frac{K_{cat} \times K C}{1 + K C} \quad (5.1)$$

Where K_{cat}, is the slow step on the surface of the photocatalyst and depend on the intensity of light. K is the adsorption coefficient of the pollutant and c is the concentration of the pollutant at time t. For the low concentration of organic pollutant, the Langmuir-Hinshelwood equation is simplified to a pseudo-first order kinetic **Equation 5.2**.

$$rate = \frac{dc}{dt} = KC \quad (5.2)$$

The integration of **Equation 5.2** result in **Equation 5.4**;

$$\ln C = \ln C_0 - Kt \quad (5.3)$$

Where K_C is the concentration at time t , C_0 is the initial concentration and k is the rate constant of the pseudo-first order. The plot of $\ln(C_0/C_t)$ against the visible light irradiation time for the photodegradation of RO 16 is shown in **Figure 5.3**. The linear relationship between the $\ln(C_0/C_t)$ and the time of visible light irradiation of all the three Au/TiO₂ composites show that the photodegradation process followed pseudo first-order kinetics as shown in **Figure 5.3**. The values of (R^2) and k were obtained directly from the linear regression of the plot of the pseudo first order and ² are shown in **Table 5.2**. The second order kinetics were also fitted, however, the correlation coefficient (R^2) showed poor correlation below 0.6587 for all the samples. The higher value of k obtained indicates the good performance of the photocatalyst. The value of $k = 0.021/\text{min}$ for the AuNRs(3.4)/TiO₂ composites indicates its good photocatalytic activity.

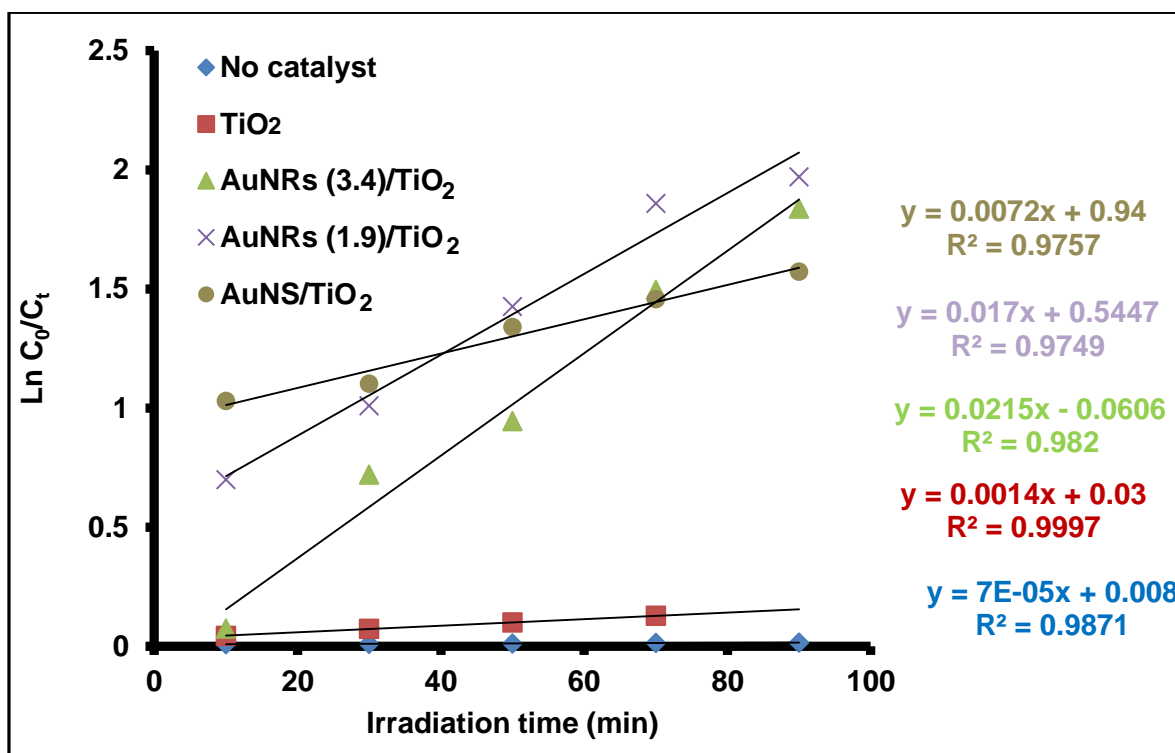


Figure 5.3: Kinetic plot of the degradation of RO 16 [$C=20$ ppm, $C_{cat}= 0.2$ g/L, $pH= 6.7$, power= 300W] AuNRs(3.4)/TiO₂, AuNRs(1.9)/TiO₂. AuNS/TiO₂, no catalyst and TiO₂.

5.4. Determination of the electrical Energy Efficiency per order (E_{EO})

Photocatalysis is an electric energy process because it uses electrical power for the process to function. The ideal process utilises less energy, therefore, the International Union of Pure and Applied Chemistry (IUPAC) suggested two figures-of-merit for the advanced oxidation processes (AOPs) on the utilization of electrical energy (Bolton et al., 2001). The suitable figure-of-merit, in the case of low pollutant concentration, is called the electrical energy per order (E_{EO}). E_{EO} is defined as the number of kilowatt-hours of electrical energy required to remove 90 % of a pollutant in 1 m³ of contaminated water (Daneshvar et al., 2005). The value of E_{EO} can be calculated using **Equations 5.4 and 5.5** below (Daneshvar et al., 2005):

$$E_{EO} = \frac{P \times t \times 1000}{V_0 \times 60 \times \log \frac{C_i}{C_f}} \quad (5.4)$$

$$E_{EO} = \frac{38.4 \times P}{V_0 \times K} \quad (5.5)$$

Where P is the power (kW) of the system, t (h) is the duration, V (m³) is the treated volume, and C_i and C_f the initial and final dye concentrations (mg/L), respectively. The values of E_{EO} are represented in **Table 5.2** below. The lowest E_{EO} of 2143 kWh/m³ was achieved when using AuNRs(3.4/TiO₂). The low value of E_{EO} further confirms that the photocatalytic process was more efficient in the presence of AuNRs (3.4)/TiO₂ compared to AuNRs (1.9)/TiO₂ and AuNS/TiO₂. Moreover, it can be deduced that the process will consume less energy, hence, reduces the cost. The achieved E_{EO} values were found to decrease in the following order: TiO₂ > AuNS/TiO₂ > AuNRs (1.9)/TiO₂ > AuNRs (3.4)/TiO₂,

Table 5.2: Photodegradation efficiency, kinetic properties and energy efficiency of RO16 using the TiO₂ AuNS/TiO₂ AuNRs (1.9)/TiO₂ and AuNRs (3.4)/TiO₂ composites.

Catalyst	Photodegradation			
	efficiency (%)	k (min ⁻¹)	R ²	E_{EO} (kWh/m ³)
TiO ₂	0.82	0.001	0.999	32914
AuNS/TiO ₂	79.24	0.007	0.976	6400
AuNRs(1.9)/TiO ₂	84.56	0.017	0.975	2710
AuNRs(3.4/TiO ₂)	86.65	0.021	0.982	2143

To summarize, the composite photocatalysts showed a good photoresponse under visible light. Moreover, the introduction of AuNPs improved the photocatalytic performance of TiO₂ for the degradation of RO 16 dye. In regard to shapes, AuNS/TiO₂ showed a lower photodegradation rate and lower efficiency compared to AuNRs/TiO₂. The degradation rate also increased as the aspect ratio of AuNRs increased. These results demonstrate that the photocatalytic activity is significantly dependent on the shape and the size of the loaded AuNPs. Furthermore, the photocatalysts prepared with AuNRs demonstrated lower E_{EO} values compared to the one with AuNS. On the basis of these results, it can be concluded that photocatalytic activity of the reported composites increases in the following order: AuNS/TiO₂ < AuNRs (1.9)/TiO₂ < AuNRs (3.4)/TiO₂.

5.2 Synergistic plasmonic effect of nanospheres and nanorods on the degradation of RO16.

In the quest to design materials with tailored light absorption properties for solar conversion, surface plasmon resonance (SPR) metals have attracted a great deal of interest. Various strategies have been developed to tune the SPR effect of the gold nanoparticles, including, tuning the aspect ratio (in nanorods), size, and shape (Gołębiewska et al., 2016, Kaur & Pal, 2012, Tanabe et al., 2015). Recently, there is also a growing interest in bimetallic metals as an alternative approach to extend the absorption of the wide band gap semiconductors towards the visible spectrum. A combination of Au-Pd, Ag-Au, Ag-Cu and Au-Cu bimetallic co-catalysts have been reported for enhanced visible light photocatalysis (Berahim et al., 2018, Ma et al., 2017, Purbia & Paria, 2017, Maniecki et al., 2009). However, the drawback of using bimetallic nanocrystals in photocatalysis is the complication of the mechanism of enhancement and low quantum efficiencies (Sytwu et al., 2019). Despite the tremendous efforts that have been made in the past to improve the light absorption of the solar spectrum, there are no reports on the mixed shapes gold nanoparticles. Herein, the synergistic effect of the two shapes (nanosphere, nanorod) was investigated. The photocatalysts were formed by first mixing an appropriate ratio of Au nanospheres and nanorods. These mixtures were then used to form the Au/TiO₂ composites using the method reported in **Section 3.4**. The prepared photocatalysts contain the ratio of AuNRs to AuNS as follows, **1:1**, **2:1** and **1:2**.

The mixture of the two shapes (rods and spheres) had a significant influence in the photodegradation and decolourisation of RO 16 as it can be seen in **Figure 6.4**. The reaction was faster in the presence of the photocatalysts that were loaded with combined shapes. Higher efficiencies may be due to the direct synergetic effect of the two different shapes resulting in the

generation of more electron/hole pairs, and thus, an improved photocatalytic process. The 1:1 and 2:1 (AuNRs to AuNS) ratio samples gave the highest efficiency of 90.15 % after 60 min of light irradiation. Meanwhile, for the 1:2 AuNS to AuNRs ratio sample a 77.07 % efficiency was achieved with the slowest degradation rate of 0.0326/min at 120 min of irradiation time. This is supported by the fact that AuNRs even with the single shape experiment gave higher degradation rates and efficiency compared to AuNS. From this experiment, it can be deduced that AuNRs are the favourable shape for coupling with the TiO₂. The combined shapes behaved better than the individual shapes (**Table 5.3**).

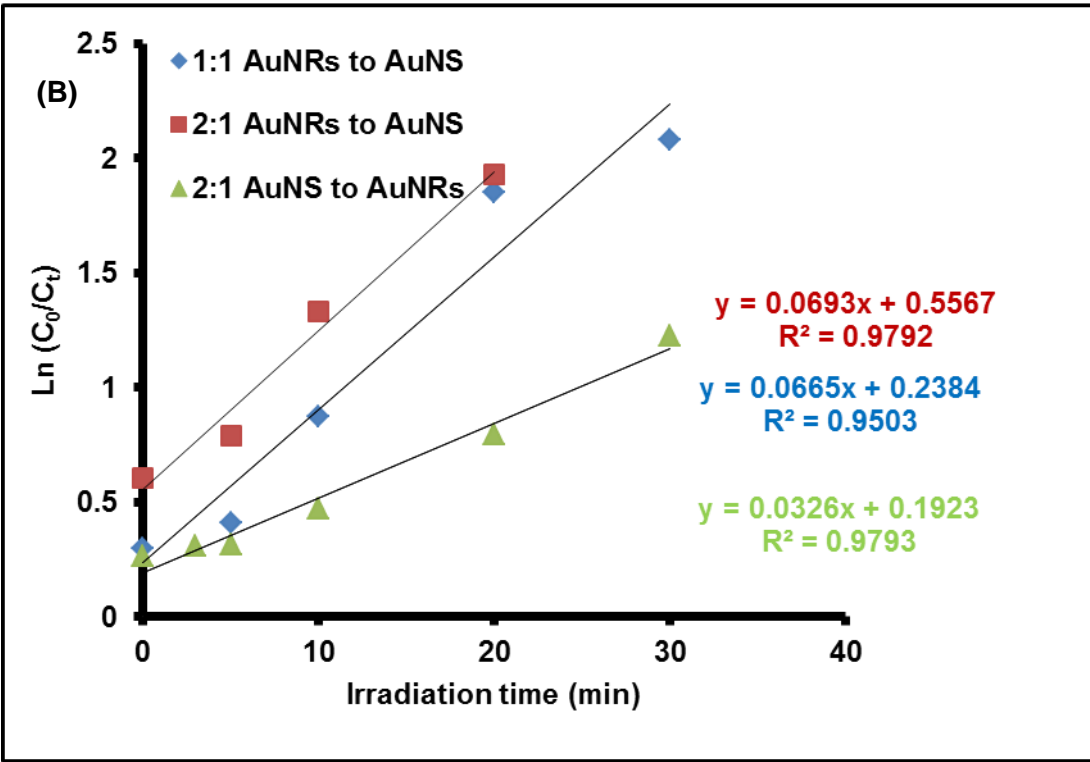
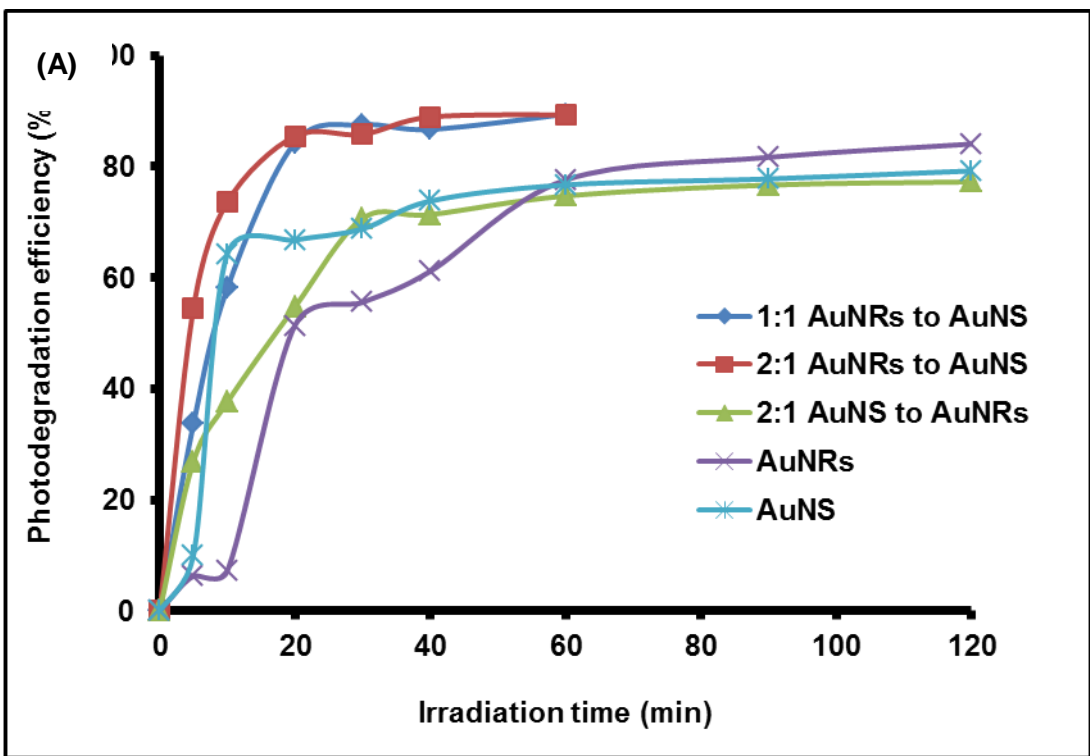


Figure 5.4: (A) Mixed shapes, AuNRs and AuNS photodegradation efficiency (B) first order kinetic of the mixed shapes effect the degradation of RO 16 [$C=20$ ppm, $C_{cat}= 0.2$ g/L, $pH= 6.7$, power= 300W] AuNRs(3.4)/TiO₂ , AuNRs(1.9)/TiO₂ . AuNS/TiO₂, no catalyst and TiO₂.

Table 5.3: Summary of varying nanospheres and nanorods ratios on the degradation of RO16.

AuNRs to AuNS (ratio)	K/min	R²	Photodegradation efficiency (%)
1:1	0.0665	0.95	90.15
2:1	0.0693	0.979	90.05
1:2	0.0326	0.979	77.89
AuNRs	0.0215	0.982	86.65
AuNS	0.0072	0.976	79.24

The results represented in **Table 5.2** for the synergetic effect of AuNS and AuNRs on the photodegradation of RO 16 showed that the mixing of the two shapes had a significant impact on both the degradation rate and the degradation efficiency percentage. It was found that when the AuNRs are in excess a higher degradation efficiency was achieved. The degradation rate decreased with the decreased of AuNRs in the mixture. The mixed shaped with AuNRs in excess was found to have the highest degradation rate, and high degradation efficiency compare to the use of AuNRs and AuNS alone as represented in **Table 5.2**.

5.3 Reusability of the photocatalyst

The recycling of the powdered photocatalysts is very important in the field of photocatalysis as it determines the stability of the catalyst. An ideal photocatalyst is the one that can be easily recycled and reused after each experiment, it should not lose its catalytic properties after usage (Padikkaparambil et al., 2013). To evaluate the reusability of AuNRs/TiO₂, the photocatalyst was separated from the reaction mixtures by centrifugation and used under the same conditions (20 ppm initial dye concentration). The achieved photodegradation efficiencies were 86.65 %, 85.78 %, 85.23 % and 79.89 %, for the first, second, third, and fourth cycles, respectively. As can be seen from these values, the photocatalyst showed good stability without any significant loss. However, the decrease in the efficiency after the fourth cycle may be due to the agglomeration of the RO 16 dye molecules on the photocatalyst surface, which reduces the adsorption of the new dye molecules in the solution.

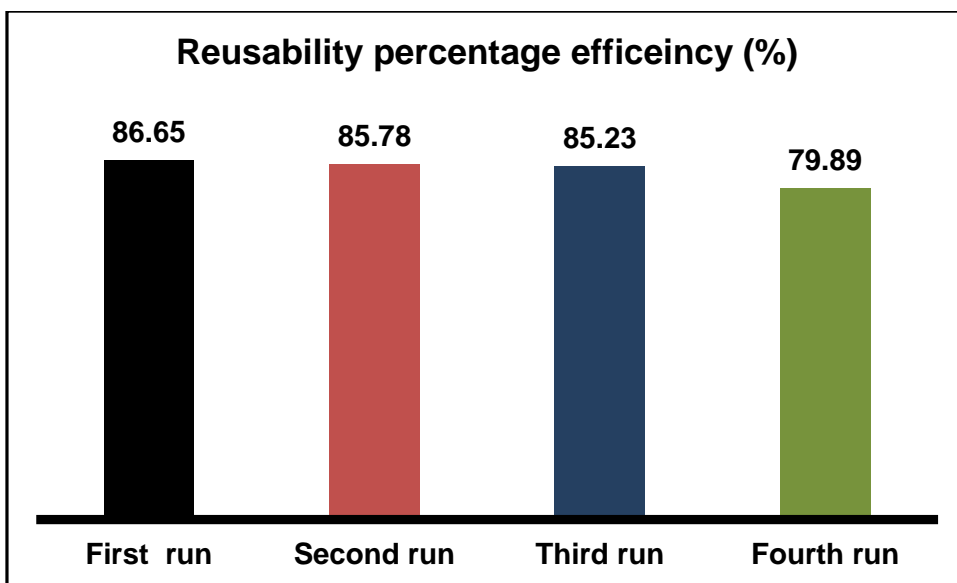


Figure 5.5: Photodegradation efficiency reusability test for RO 16 [C=20 ppm, Ccat= 0.2 g/L, pH= 6.7, power= 300W] AuNRs (3.4)/TiO₂

CHAPTER 6

EFFECT OF OPERATIONAL PARAMETERS ON THE PHOTOCATALYTIC DEGRADATION OF RO 16

This chapter discusses the results on the effect of operational parameters which affect the photocatalytic performance of the Au/TiO₂ photocatalyst. The factors investigated in this project include the loading of the gold onto TiO₂, the pH of the dye solution and the temperature of the dye solution. Based on the results in Chapter 5, the photocatalyst used to study the parameters was AuNRs (3.4/TiO₂).

6.1 Effect of Au loading in Au/TiO₂ nanocomposites

The photocatalytic performance of AuNRs/TiO₂ nanocomposites was evaluated at different Au loadings, in the range of 0.1 wt % to 0.4 wt %. It was observed that increasing the Au loading from 0.1 wt % Au to 0.2 wt %, increased the photocatalytic degradation and decolourization of RO 16 from 56.29 % to 86.65 % respectively, as shown in **Figure 6.1**. The increase in the rate of the reaction from 0.066/min to 0.021/min in 0.2 wt % loading (**Table 6.1**) can be attributed to the formation of more crystalline imperfections formed on the surface of TiO₂. These defects cause the generation of more hot spots, which subsequently result in an increase of generation of electron/holes on the surface of the catalyst (Hsiao et al., 2011). However, a further increase in Au loading to 0.4 wt % resulted in a decrease in the degradation efficiency to 66.35 %. The reduction in the rate of the reaction is due to the reduced penetration of light onto TiO₂ because of the excess Au particles on the TiO₂ surface. Similar results were observed by Bumajdad and co-workers (2013) who reported that, by increasing the content of Au on TiO₂, there was an increase in the photodegradation rate of saframin-O dye. But, when the amount of Au loaded was further increased, the photocatalytic performance of TiO₂ decreased due to the high content of Au particles on the surface of TiO₂ which may reduce the surface accessibility for photons (Bumajda et al., 2013). The summary of these results is reported in **Table 6.1**.

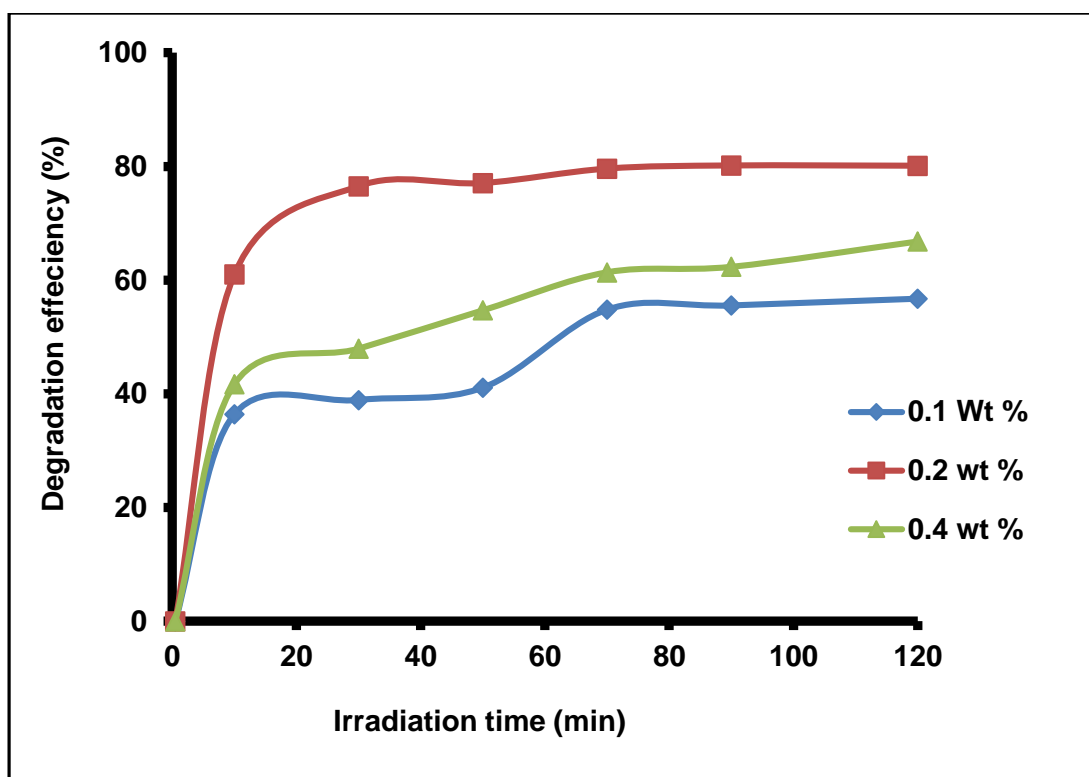


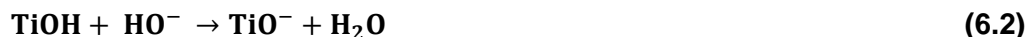
Figure 6.1: Effect of Au loading in Au/TiO₂ on the photocatalytic degradation efficiency of RO 16. [C=20 ppm, C_{cat}= 0.2 g/L, pH= 6.7, power= 300W].

Table 6.1: Effect of Au loading onto/TiO₂ on the photodegradation of RO 16 .

Au wt %	K/min	R ²	Photodegradation efficiency (%)
0.1	0.007	0.955	56.29
0.2	0.021	0.982	86.65
0.4	0.006	0.972	66.35

6.2 Effect of pH on the degradation of RO16

pH is one of the most important parameters that affect the photocatalytic degradation because it determines the adsorption of dyes onto the surface of the catalyst (Ajmal et al., 2014). In an acidic medium, the surface of the catalyst is usually positively charged. However, in basic medium deprotonation takes place on the surface of the catalyst because of the negative charge of hydroxyl radical. **Equations 6.1** and **6.2** show the protonation and deprotonation of the catalyst (Kumar et al., 2017).



Different researchers have reported that when the pH of the solution is lower than the point zero charges of TiO_2 , which is at pH 6.8, the surface of TiO_2 will be positively charged (Kumar et al., 2017, Ajimal et al., 2014, Alaton et al., 2002). To study the effect of pH, the degradation of RO 16 was performed at pH 2.5 to pH 11.5 and the results are presented in **Figure 6.2**. Sodium hydroxide (NaOH) and hydrochloric acid (HCl) were used to adjust the pH in the solution. **Figure 6.2** shows that an increase in pH from 2.5 to 6.7 caused the degradation efficiency to increase from 25.02 % to 86.65 %. However, the opposite trend was observed at pH higher than 6.7. The results reveal that from pH 8.0 to 11.5, the degradation efficiency decreased from 75.23 % to 66.56%. The excess of HO^- in the solution may cause the decrease in efficiency, because of the competition on the adsorption of RO 16 and HO^- onto the surface of the catalyst (Kumar et al., 2017). Moreover, because of the excess HO^- the surface of the catalyst is negatively charged and that may cause coulombic repulsion between the negative charge on RO 16 and the negative charge of the catalyst. The highest degradation efficiency was observed at pH 6.7, which was the pH of the RO 16 solution.

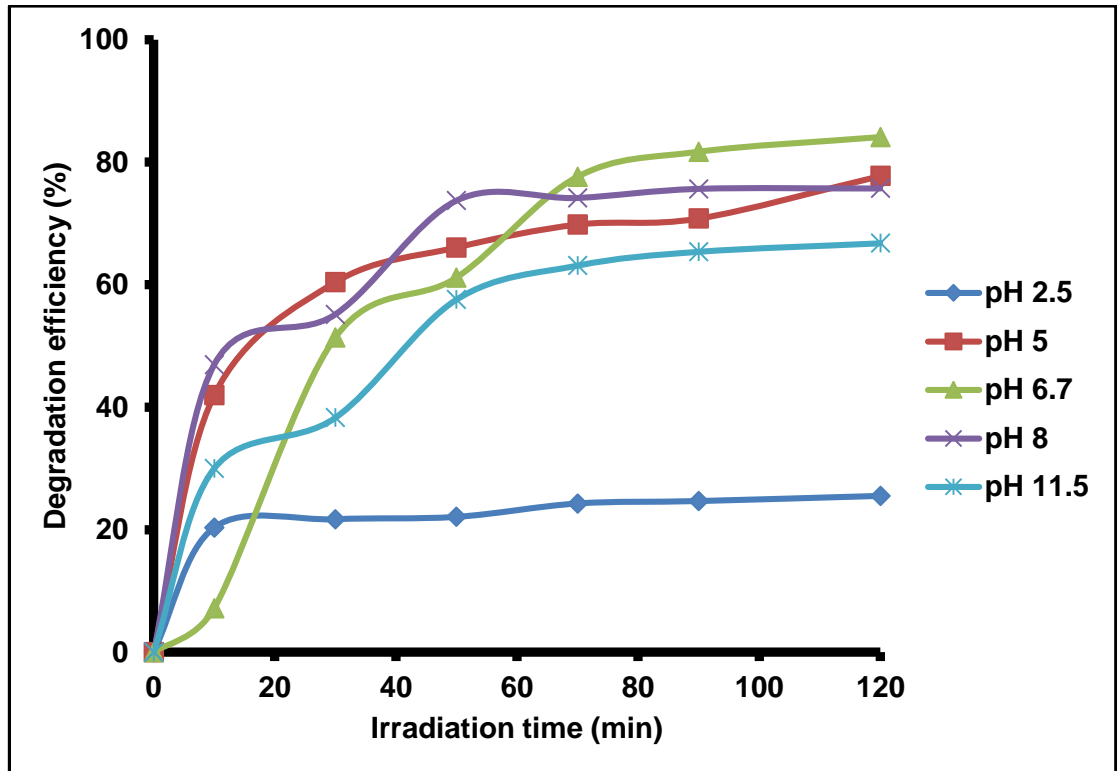


Figure 6.2: Degradation efficiency percentage of the effect of pH on RO 16 decolourisation, and degradation [C=20 ppm, Ccat= 0.2 g/L, pH= 6.7, power= 300W].

The slower rate of RO 16 photodegradation at pH 2.5 (0.007/min) reported in **Table 6.2** may be due to the agglomeration of TiO₂ particles, which are capable of reducing the surface area of TiO₂ for photon adsorption and RO 16 adsorption onto TiO₂ (Ajmal et al., 2014). However, Sakthivel and co-workers (2003) reported a maximum degradation efficiency and faster rate in the degradation of acid yellow 17 anionic dyes at pH 3. It can be said that different anionic dyes have different adsorption strength onto the surface of the catalyst. Therefore, it can be argued that there is no certainty that anionic dyes would always have high degradation efficiencies at lower pH or an acidic medium. In this regard, Muruganandham & Swaminathan (2004) reported that in the degradation of reactive orange 4 (anionic dye), the rate and the degradation efficiency increase from 25 % to 90 % between pH 1 to pH 9. In this study, the highest degradation and decolourisation rate and efficiency of RO 16 were observed at pH 6.7.

Table 6.2 Summary of the photodegradation data with a change in pH using Au/TiO₂ nanocomposites (0.2 g/L) with RO 16 (20 ppm).

pH	K/min	R ²	Photodegradation efficiency (%)
2.5	0.0007	0.967	25.02
5	0.0120	0.969	77.18
6.7	0.0215	0.982	86.65
8	0.0117	0.937	75.23
11.5	0.0101	0.956	66.56

6.3. Effect of temperature

Previous studies have shown that the temperature of the solution affects the photocatalytic degradation of dyes. Kumar & Pandey (2017) reported an increase of the efficiency from 76 % to 88 % when the temperature was raised from 30 °C to 40 °C respectively for, the degradation of methyl orange. However, a further increase in temperature above 80 °C, favoured the recombination of electrons-holes pairs, hence, reducing the adsorption of organic molecules on the surface of TiO₂ (Kumar et al., 2017). In this study, the reaction temperature had a significant effect on the photodegradation of RO 16 under visible light. The degradation efficiency was found to increase from 55.09 % to 86.65 % when the temperature was raised from 15 °C to 30 °C, respectively. The rate of the RO 16 degradation decreased with a decrease in temperature from 0.021/min to 0.008/min as shown in **Table 6.3**. The rate of reaction was almost 3 times faster at 30 °C compared to 15 °C because the decrease in temperature results in an increase in the activation energy, and that means more energy would be required for the activation of TiO₂ (Kumar et al., 2017).

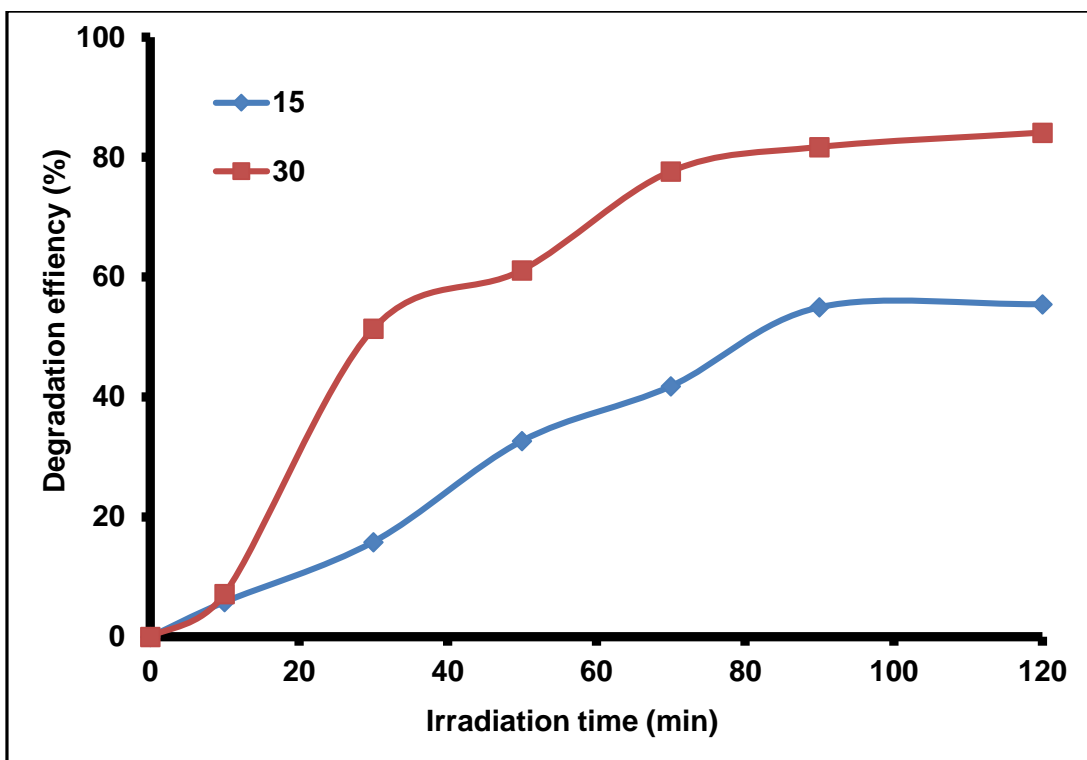


Figure 6.3: Effect of temperature on the photocatalytic degradation efficiency of RO 16 [C= 20 ppm, C_{cat} (Au/TiO₂) = 0.2 g/L, pH= 6.7, power= 300 W.

In summary, the results of the photodegradation of RO 16 using Au/TiO₂ show that the loading of Au onto TiO₂ increases the rate of the reaction and the amount of Au increased; however, a further increase of Au resulted in a decrease in the reaction rate. The rate of the degradation of RO 16 decreased as the temperature of the solution decreased. The pH of the solution increased the rate of the reaction when the pH increased in the acidic medium and the opposite trend was observed in a basic medium.

CHAPTER 7

CONCLUSIONS AND RECOMMENDATIONS

7.1 Conclusions

In this study, AuNS/TiO₂, AuNRs (1.9)/TiO₂ and AuNRs (3.4)/TiO₂ nanocomposite photocatalysts were successfully synthesised and characterised. The results from the optical and structural characterisation confirmed the presence of both AuNPs and TiO₂ in the composite materials. The TEM and SEM results also confirmed the desired shapes and formation of Au/TiO₂ nanocomposite.

The results of this study highlight the role of Au nanoparticles in enhancing the photocatalytic activity of TiO₂ under visible light. In this work, three Au/TiO₂ nanocomposites were prepared, using spherical (AuNS), and rod-shaped (AuNRs) with different aspect ratios (1.9 and 3.4), and their effect on the photocatalytic degradation of RO 16 was investigated. The photocatalyst loaded with AuNRs demonstrated the highest degradation efficiency of 86.65 % compared to 79.24 % for the one loaded with AuNSs after 120 minutes of light irradiation. The highest photodegradation efficiency was achieved for the photocatalyst with AuNRs (3.4) compared to AuNRs (1.9) due to the larger surface area. This result shows that the aspect ratio affected the photodegradation of RO 16 dye. The photocatalytic degradation of RO 16 followed pseudo first order kinetics.

The photocatalytic degradation was significantly enhanced when the nanorods and nanospheres were mixed together. These catalysts demonstrated higher efficiency compared to the catalysts that were prepared with individual shapes. The achieved degradation efficiency for 1:1 and 2:1 (ratio of AuNRs to AuNS) was 90.15 % and 90.05 %, respectively. For the 1:2 photocatalyst the degradation efficiency was 77.89 %. The results show a significant effect of the mixed shapes in the preparation of plasmon-based photocatalysts. It was evident from these results that the rod-shaped AuNPs had a greater impact in enhancing the photocatalytic activity

The effects of different parameters such as pH, temperature, AuNPs loading were also investigated. It was shown that in very acidic (pH 2.5) and very basic (pH 11), the photocatalytic efficiency of the degradation of RO 16 decreased due to the increased concentration of the OH⁻ ions in the solution. However, the degradation of RO 16 was higher at conditions between pH 6 and 7. The photocatalytic efficiency significantly increased with gold loading onto TiO₂ from 0.1 wt % to 0.2 wt %. However, a gradual decrease was observed with a further increase to 0.4 wt % due to the lower penetration of light on the surface of the photocatalyst. The temperature on

the performance of photocatalyst was investigated at 15 °C and 30 °C. The rate of degradation of RO 16 was found to increase with an increase in temperature. This increase in the degradation rate was due to the increase in the activation energy. The results from the reusability tests show that the photocatalyst can be recycled and re-used with an efficiency of 79.89 % after four cycles.

7.2 Recommendations

This work highlights a significant potential of the Au/TiO₂ photocatalysts on plasmon-enhanced photocatalyst in the treatment of azo dyes in water using the visible light. Future studies may be devoted to the following:

- More work is required in finding simple methods for the production of photocatalysts on a large scale.
- Studies can be done on the immobilization of these photocatalysts to facilitate easy removal and re-use
- Future research should also be done on the effect of mixed shapes for a better understanding of the mechanism of the synergistic effect of AuNPs with different shapes.
- Additionally, these studies can be done in real textile wastewater.

REFERENCES

- Agegnehu, A., Pan, C., Tsai, M., Rick, J., Su, W., Lee, J. & Hwang, B. 2016. Visible light responsive noble metal-free nanocomposite of V-doped TiO₂ nanorod with highly reduced graphene oxide for enhanced solar H₂ production. *International Journal of Hydrogen Energy*, 41(16): 6752-6762.
- Alaton, I., Balcioglu, I. & Bahnemann, D. 2002. Advanced oxidation of a reactive dye bath effluent: comparison of O₃, H₂O₂/UV-C and TiO₂/UV-A processes. *Water Research*, 36(5): 1143-1154.
- Ali, I., Suhail, M., Alothman, Z. & Alwarthan, A. 2018. Recent advances in syntheses, properties and applications of TiO₂ nanostructures. *RSC Advances*, 8(53): 30125-30147.
- Alshammari, A., Bagabas, A. & Assulami, M. 2014. Photodegradation of rhodamine B over semiconductor supported gold nanoparticles: The effect of semiconductor support identity. *Arabian Journal of Chemistry*.
- Ananthashankar, A. 2013. Production, Characterization and Treatment of Textile Effluents: A Critical Review. *Journal of Chemical Engineering & Process Technology*, 05(01).
- Anouar, H., Anouar, E., El Hourch, A. & El Kacemi, K. 2014. *Electronic and Optical Properties of Reactive Orange 16 azo dye*. 8th ed. International Journal of Innovation and Applied Studies.
- Ajmal, A., Majeed, I., Malik, R., Idriss, H. & Nadeem, M. 2014. Principles and mechanisms of photocatalytic dye degradation on TiO₂ based photocatalysts: a comparative overview. *RSC Adv.*, 4(70): 37003-37026.
- Ansari, S., Khan, M., Ansari, M. & Cho, M. 2016. ChemInform Abstract: Nitrogen-Doped Titanium Dioxide (N-Doped TiO₂) for Visible Light Photocatalysis. *ChemInform*, 47(25).
- Araña, J., Fernández Rodríguez, C., González Díaz, O., Herrera Melián, J. & Pérez Peña, J. 2005. Role of Cu in the Cu-TiO₂ photocatalytic degradation of dihydroxybenzenes. *Catalysis Today*, 101(3-4): 261-266.
- Arshad, M., Trafela, Š., Rožman, K., Kovač, J., Djinović, P. & Pintar, A. 2017. Determination of Schottky barrier height and enhanced photoelectron generation in novel plasmonic

- immobilized multisegmented (Au/TiO₂) nanorod arrays (NRAs) suitable for solar energy conversion applications. *Journal of Materials Chemistry C*, 5(40): 10509-10516.
- Asahi, R. 2001. Visible-Light Photocatalysis in Nitrogen-Doped Titanium Oxides. *Science*, 293(5528): 269-271.
- Ayati, A., Ahmadpour, A., Bamoharram, F., Tanhaei, B., Mänttari, M. & Sillanpää, M. 2014. A review on catalytic applications of Au/TiO₂ nanoparticles in the removal of water pollutant. *Chemosphere*, 107: 163-174.
- Bannat, I., Wessels, K., Oekermann, T., Rathousky, J., Bahnemann, D. and Wark, M. (2009). Improving the Photocatalytic Performance of Mesoporous Titania Films by Modification with Gold Nanostructures. *Chemistry of Materials*, 21(8), pp.1645-1653.
- Bansal, P., Singh, D. & Sud, D. 2009. Comparative Evaluation of UV/ Solar Light Induced Photodegradation of Azo Dye in Aqueous Solutions. *Asian Journal of Chemistry*, 21(10): 287-291.
- Berahir, N., Basirun, W., Leo, B. & Johan, M. 2018. Synthesis of Bimetallic Gold-Silver (Au-Ag) Nanoparticles for the Catalytic Reduction of 4-Nitrophenol to 4-Aminophenol. *Catalysts*, 8(10): 412.
- Berthomieu, C. & Hienerwadel, R. 2009. Fourier transform infrared (FTIR) spectroscopy. *Photosynthesis Research*, 101(2-3): 157-170.
- Bumajdad, A., Madkour, M., Abdel-Moneam, Y. & El-Kemary, M. 2013. Nanostructured mesoporous Au/TiO₂ for photocatalytic degradation of a textile dye: the effect of size similarity of the deposited Au with that of TiO₂ pores. *Journal of Materials Science*, 49(4): 1743-1754.
- Bunaciu, A., Udriștioiu, E. & Aboul-Enein, H. 2015. X-Ray Diffraction: Instrumentation and Applications. *Critical Reviews in Analytical Chemistry*, 45(4): 289-299.
- Bolton, J., Bircher, K., Tumas, W. & Tolman, C. 2001. Figures-of-merit for the technical development and application of advanced oxidation technologies for both electric- and solar-driven systems (IUPAC Technical Report). *Pure and Applied Chemistry*, 73(4): 627-637.
- Bora, L. V. & Mewada, R.K., 2017. Visible/solar light active photocatalysts for organic effluent treatment: Fundamentals, mechanisms and parametric review. *Renewable and Sustainable Energy Reviews*, 76(January), pp.1393–1421.

- Brust, M., Walker, M., Bethell, D., Schiffrin, D. & Whyman, R. 1994. Synthesis of thiol-derivatised gold nanoparticles in a two-phase Liquid–Liquid system. *J. Chem. Soc., Chem. Commun.*, 0(7): 801-802.
- Chen, H., Shao, L., Li, Q. & Wang, J. 2013. Gold nanorods and their plasmonic properties. *Chem. Soc. Rev.*, 42(7): 2679-2724.
- Chen, J., Saeki, F., Wiley, B., Cang, H., Cobb, M., Li, Z., Au, L., Zhang, H., Kimmey, M., Li & Xia, Y. 2005. Gold Nanocages: Bioconjugation and Their Potential Use as Optical Imaging Contrast Agents. *Nano Letters*, 5(3): 473-477.
- Chong, M., Jin, B., Chow, C. & Saint, C. 2010. Recent developments in photocatalytic water treatment technology: A review. *Water Research*, 44(10): 2997-3027.
- Daneshvar, N., Aleboye, A. & Khataee, A. 2005. The evaluation of electrical energy per order (EEo) for photooxidative decolorization of four textile dye solutions by the kinetic model. *Chemosphere*, 59(6): 761-767.
- Das, M., Shim, K., An, S. & Yi, D. 2011. Review on gold nanoparticles and their applications. *Toxicology and Environmental Health Sciences*, 3(4): 193-205.
- Delannoy, L., El Hassan, N., Musi, A., Le To, N., Krafft, J. & Louis, C. 2006. Preparation of Supported Gold Nanoparticles by a Modified Incipient Wetness Impregnation Method. *The Journal of Physical Chemistry B*, 110(45): 22471-22478.
- Di Paola, A., Bellardita, M. & Palmisano, L. 2013. Brookite, the Least Known TiO₂ Photocatalyst. *Catalysts*, 3(1): 36-73.
- Di Valentin, C., Pacchioni, G. & Selloni, A. 2005. Theory of Carbon Doping of Titanium Dioxide. *Chemistry of Materials*, 17(26): 6656-6665.
- Flores, N., Pal, U., Galeazzi, R. & Sandoval, A. 2014. Effects of morphology, surface area, and defect content on the photocatalytic dye degradation performance of ZnO nanostructures. *RSC Adv.*, 4(77): 41099-41110.
- Fujishima, A. & Honda, K. 1972. Electrochemical Photolysis of Water at a Semiconductor Electrode. *Nature*, 238(5358): 37-38.
- Garg, A. & Tomar, G. 2013. Short Review on Application of Gold Nanoparticles. *Global Journal of Pharmacology*, 1(7): 34-38.

- Gillespie, A., Jao, D., Andriola, A., Duda, T., Yang, C. & Yu, L. 2012. Gold Nanoparticle Determination by Inductively Coupled Plasma-Mass Spectrometry, Anodic Stripping Voltammetry, and Flame Atomic Absorption Spectrophotometry. *Analytical Letters*, 45(10): 1310-1320.
- Gołębiewska, A., Malankowska, A., Jarek, M., Lisowski, W., Nowaczyk, G., Jurga, S. & Zaleska-Medynska, A. 2016. The effect of gold shape and size on the properties and visible light-induced photoactivity of Au-TiO₂. *Applied Catalysis B: Environmental*, 196: 27-40.
- Herrmann, J. 1999. Heterogeneous photocatalysis: fundamentals and applications to the removal of various types of aqueous pollutants. *Catalysis Today*, 53(1): 115-129.
- Hossein-Babaei, F., Lajvardi, M. & Alaei-Sheini, N. 2015. The energy barrier at noble metal/TiO₂ junctions. *Applied Physics Letters*, 106(8): 083503.
- Holkar, C., Jadhav, A., Pinjari, D., Mahamuni, N. & Pandit, A. 2016. A critical review on textile wastewater treatments: Possible approaches. *Journal of Environmental Management*, 182: 351-366.
- Hou, W., Liu, Z., Pavaskar, P., Hung, W. and Cronin, S. (2011). Plasmonic enhancement of photocatalytic decomposition of methyl orange under visible light. *Journal of Catalysis*, 277(2), pp.149-153.
- Hou, X. & Jones, B. 2000. Inductively Coupled Plasma/Optical Emission Spectrometry. *Encyclopedia of Analytical Chemistry*: 9468-9485.
- Hsiao, R., Roselin, L., Hsu, H., Selvin, R. & Juang, R. 2011. Photocatalytic degradation of reactive orange 16 dye over Au-doped TiO₂ in aqueous suspension. *Int. J. Materials Engineering Innovation*, 2(1): 96-108
- Ibhadon, A. & Fitzpatrick, P. 2013. Heterogeneous Photocatalysis: Recent Advances and Applications. *Catalysts*, 3(1): 189-218.
- Jagdale, T., Kulkarni, M., Pravarthana, D., Ramadan, W. & Thakur, P. 2012. Photocatalytic Degradation of Azo Dyes Using Au:TiO₂, γ -Fe₂O₃:TiO₂ Functional Nanosystems. *Journal of Nanoscience and Nanotechnology*, 12(2): 928-936.
- Kaur, R. & Pal, B. 2012. Size and shape dependent attachments of Au nanostructures to TiO₂ for optimum reactivity of Au-TiO₂ photocatalysis. *Journal of Molecular Catalysis A: Chemical*, 355: 39-43

- Karimi, L., Zohoori, S. & Yazdanshenas, M. 2014. Photocatalytic degradation of azo dyes in aqueous solutions under UV irradiation using nano-strontium titanate as the nanophotocatalyst. *Journal of Saudi Chemical Society*, 18(5): 581-588.
- Khan, M., Adil, S. & Al-Mayouf, A. 2015. Metal oxides as photocatalysts. *Journal of Saudi Chemical Society*, 19(5): 462-464.
- Khoa, N., Kim, S., Yoo, D., Kim, E. & Hahn, S. 2014. Size-dependent work function and catalytic performance of gold nanoparticles decorated graphene oxide sheets. *Applied Catalysis A: General*, 469: 159-164.
- Kimling, J., Maier, M., Okenve, B., Kotaidis, V., Ballot, H. & Plech, A. 2006. Turkevich Method for Gold Nanoparticle Synthesis Revisited. *The Journal of Physical Chemistry B*, 110(32): 15700-15707.
- Kumar, S. 2006. *Spectroscopy of Organic Compounds*.
http://www.uobabylon.edu.iq/eprints/publication_11_8282_250.pdf 12 December 2018.
- Kumar, A. 2017. A Review on the Factors Affecting the Photocatalytic Degradation of Hazardous Materials. *Material Science & Engineering International Journal*, 1(3).
- Kumar, A. & Pandey, G. 2017. Photodegradation of Methyl Orange in Aqueous Solution by the Visible Light Active Co:La:TiO₂ Nanocomposite. *Chemical Sciences Journal*, 08(03).
- Kumar, D., Meenan, B., Mutreja, I., D'sa, R. & Dixon, D. 2012. controlling the size and size distribution of gold nanoparticles: a design of experiment study. *International Journal of Nanoscience*, 11(02): 1250023
- Kumar, D., Park, C. & Kim, C. 2017. Plasmon Assisted and Visible Light Irradiated Efficient Organic Pollutants Degradation. *international journal of advance research in science and engineering*, 6(10): 1576-1582.
- Kirkland, A., Kim, J., Warner, J., Borisenko, K., Haigh, S., Young, N., Wang, P. & Nellist, P. 2014. Applications of Aberration Corrected TEM and Exit Wavefunction Reconstruction to Materials Science. *Microscopy and Microanalysis*, 20(S3): 930-931.
- Kwiatkowski, M., Chassagnon, R., Heintz, O., Geoffroy, N., Skompska, M. & Bezverkhyy, I. 2017. Improvement of photocatalytic and photoelectrochemical activity of ZnO/TiO₂ core/shell system through additional calcination: Insight into the mechanism. *Applied Catalysis B: Environmental*, 204: 200-208.

- Latha, A., Oviya, T. & Sandhiya, K. 2018. Treatment Technologies of Textile Dyeing Effluent A Review. *International Journal of Engineering Research and*, V6(02).
- Lee, S., Lintang, H. & Yuliati, L. 2017. High photocatalytic activity of Fe₂O₃/TiO₂ nanocomposites prepared by photodeposition for degradation of 2,4-dichlorophenoxyacetic acid. *Beilstein Journal of Nanotechnology*, 8: 915-926.
- Lee, S. & Park, S. 2013. TiO₂ photocatalyst for water treatment applications. *Journal of Industrial and Engineering Chemistry*, 19(6): 1761-1769.
- León, A., Reuquen, P., Garín, C., Segura, R., Vargas, P., Zapata, P. & Orihuela, P. 2017. FTIR and Raman Characterization of TiO₂ Nanoparticles Coated with Polyethylene Glycol as Carrier for 2-Methoxyestradiol. *Applied Sciences*, 7(1): 49.
- Li, B., Gu, T., Ming, T., Wang, J., Wang, P., Wang, J. & Yu, J. 2014. (Gold Core)@(Ceria Shell) Nanostructures for Plasmon-Enhanced Catalytic Reactions under Visible Light. *ACS Nano*, 8(8): 8152-8162.
- Li, G., Chen, L., Dimitrijevic, N. & Gray, K. 2008. Visible light photocatalytic properties of anion-doped TiO₂ materials prepared from a molecular titanium precursor. *Chemical Physics Letters*, 451(1-3): 75-79.
- Li, J. & Zeng, H. 2006. Preparation of Monodisperse Au/TiO₂ Nanocatalysts via Self-Assembly. *Chemistry of Materials*, 18(18): 4270-4277.
- Liu, T. et al., 2017. Au/ZnO nanoarchitectures with Au as both supporter and antenna of visible-light. *Applied Surface Science*, 392, pp.616–623
- Liu, L., Ouyang, S. & Ye, J. 2013. Gold-Nanorod-Photosensitized Titanium Dioxide with Wide-Range Visible-Light Harvesting Based on Localized Surface Plasmon Resonance. *Angewandte Chemie International Edition*, 52(26): 6689-6693.
- Lindströma, B. & Pettersson, L. 2003. A brief history of catalysis. , 7(4).
- López-Vásquez, A., Santamaría, D., Tibatá, M. & Gómez, C. 2010. Congo Red Photocatalytic Decolourization using Modified Titanium. *International Journal of Environmental and Earth Sciences*, 1:2.
- Luo, S., Xiao, Y., Yang, L., Liu, C., Su, F., Li, Y., Cai, Q. & Zeng, G. 2011. Simultaneous detoxification of hexavalent chromium and acid orange 7 by a novel Au/TiO₂ heterojunction composite nanotube arrays. *Separation and Purification Technology*, 79(1): 85-91.

- Lu, K., Zhang, X., Zhao, Y. & Wu, Z. 2010. Removal of color from textile dyeing wastewater by foam separation. *Journal of Hazardous Materials*, 182(1-3): 928-932.
- Lu, Y., Chen, S., Quan, X. & Yu, H. 2011. Fabrication of a TiO₂/Au Nanorod Array for Enhanced Photocatalysis. *Chinese Journal of Catalysis*, 32(11-12): 1838-1843.
- Malik, R., Chaudhary, V., Tomer, V., Rana, P., Nehra, S. & Duhan, S. 2016. Visible light-driven mesoporous Au–TiO₂/SiO₂ photocatalysts for advanced oxidation process. *Ceramics International*, 42(9): 10892-10901.
- Ma, T., Liang, F., Chen, R., Liu, S. & Zhang, H. 2017. Synthesis of Au-Pd Bimetallic Nanoflowers for Catalytic Reduction of 4-Nitrophenol. *Nanomaterials*, 7(9): 239.
- Maniecki, T., Mierczynski, P., Maniukiewicz, W., Bawolak, K., Gebauer, D. & Jozwiak, W. 2009. Bimetallic Au–Cu, Ag–Cu/CrAl₃O₆ Catalysts for Methanol Synthesis. *Catalysis Letters*, 130(3-4): 481-488.
- Michalska, Z. & Webster, D. 1974. Supported Homogeneous Catalysts transition metal complexes with polymeric ligands. *platinum Metals rev*, 2(18): 65-73.
- Mirkhani, V., Tangestaninejad, S., Moghadam, M., Habibi, M. & Rostami-Vartooni, A. 2009. Photocatalytic degradation of azo dyes catalyzed by Ag doped TiO₂ photocatalyst. *Journal of the Iranian Chemical Society*, 6(3): 578-587.
- Moon, J., Lee, S. & Joo, J. 2018. Controllable one-pot synthesis of uniform colloidal TiO₂ particles in a mixed solvent solution for photocatalysis. *Beilstein Journal of Nanotechnology*, 9: 1715-1727.
- Murcia Mesa, J. 2017. Methylene blue degradation over M-TiO₂ photocatalysts (M= Au or Pt). *ciencia en desarrollo*, 8(1).
- Muruganandham, M. & Swaminathan, M. 2004. Solar photocatalytic degradation of a reactive azo dye in TiO₂-suspension. *Solar Energy Materials and Solar Cells*, 81(4): 439-457.
- Naik, G., Mishra, P. & Parida, K. 2013. Green synthesis of Au/TiO₂ for effective dye degradation in aqueous system. *Chemical Engineering Journal*, 229: 492-497.
- Orendorff, C. & Murphy, C. 2006. Quantitation of Metal Content in the Silver-Assisted Growth of Gold Nanorods. *The Journal of Physical Chemistry B*, 110(9): 3990-3994.
- Ostwald, W. 1902. Nobel Lecture on catalysis.

- Padikkaparambil, S., Narayanan, B., Yaakob, Z., Viswanathan, S. & Tasirin, S. 2013. Au/TiO₂ Reusable Photocatalysts for Dye Degradation. *International Journal of Photoenergy*, 2013: 1-10.
- Peichang, D., Jiezhen, H., Haizeng, W. & Baowei, S. 2010. Hydrothermal Preparation and Comparative Study of Halogen-doping TiO₂ Photocatalysts. *Journal of Advanced Oxidation Technologies*, 13(2).
- Pei, C. & Leung, W. 2013. Photocatalytic degradation of Rhodamine B by TiO₂/ZnO nanofibers under visible-light irradiation. *Separation and Purification Technology*, 114: 108-116.
- Perala, S. & Kumar, S. 2013. On the Mechanism of Metal Nanoparticle Synthesis in the Brust-Schiffrin Method. *Langmuir*, 29(31): 9863-9873.
- Perkgoz, N., Toru, R., Unal, E., Sefunc, M., Tek, S., Mutlugun, E., Soganci, I., Celiker, H., Celiker, G. & Demir, H. 2011. Photocatalytic hybrid nanocomposites of metal oxide nanoparticles enhanced towards the visible spectral range. *Applied Catalysis B: Environmental*, 105(1-2): 77-85.
- Petryayeva, E. & Krull, U. 2011. Localized surface plasmon resonance: Nanostructures, bioassays and biosensing—A review. *Analytica Chimica Acta*, 706(1): 8-24.
- Prati, L. & Villa, A. 2011. The Art of Manufacturing Gold Catalysts. *Catalysts*, 2(1): 24-37.
- Purbia, R. & Paria, S. 2017. An Au/AgBr–Ag heterostructure plasmonic photocatalyst with enhanced catalytic activity under visible light. *Dalton Transactions*, 46(3): 890-898.
- Rajeshwar, K. 1995. Photoelectrochemistry and the environment. *Journal of Applied Electrochemistry*, 25(12).
- Ranga, S. 2017. Comparative Analysis of Homogeneous and Heterogeneous Catalysis. *International Journal of Engineering Technology Science and Research*, 4(9): 1496-1500.
- Rauf, M., Meetani, M. & Hisaindee, S. 2011. An overview on the photocatalytic degradation of azo dyes in the presence of TiO₂ doped with selective transition metals. *Desalination*, 276(1-3): 13-27.
- Reyes-Coronado, D., Rodríguez-Gattorno, G., Espinosa-Pesqueira, M., Cab, C., de Coss, R. & Oskam, G. 2008. Phase-pure TiO₂ nanoparticles: anatase, brookite and rutile. *Nanotechnology*, 19(14): 145605.

- Rostami-Vartooni, A., Nasrollahzadeh, M., Salavati-Niasari, M. & Atarod, M. 2016. Photocatalytic degradation of azo dyes by titanium dioxide supported silver nanoparticles prepared by a green method using *Carpobrotus acinaciformis* extract. *Journal of Alloys and Compounds*, 689: 15-20.
- Roy Choudhury, A. 2018. Eco-friendly curcumin-based dyes for supercritical carbon dioxide natural fabric dyeing. *Advanced Materials and Technologies for Environmental Application*, 1(2):145-176.
- Rupa, A., Manikandan, D., Divakar, D. & Sivakumar, T. 2007. Effect of deposition of Ag on TiO₂ nanoparticles on the photodegradation of Reactive Yellow-17. *Journal of Hazardous Materials*, 147(3): 906-913.
- Sakthivel, S., Neppolian, B., Shankar, M., Arabindoo, B., Palanichamy, M. & Murugesan, V. 2003. Solar photocatalytic degradation of azo dye: comparison of photocatalytic efficiency of ZnO and TiO₂. *Solar Energy Materials and Solar Cells*, 77(1): 65-82.
- Scholten, J. 1985. Heterogeneous catalysis. *Applied Catalysis*, 16(1): 130-132.
- Shajari, D., Bahari, A., Gill, P. & Mohseni, M. 2017. Synthesis and tuning of gold nanorods with surface plasmon resonance. *Optical Materials*, 64: 376-383.
- Shang, J. & Gao, X. 2014. Nanoparticle counting: towards accurate determination of the molar concentration. *Chem. Soc. Rev.*, 43(21): 7267-7278.
- Sharma, S. & Bhattacharya, A. 2016. Drinking water contamination and treatment techniques. *Applied Water Science*, 7(3): 1043-1067.
- Sharma, V., Park, K. & Srinivasarao, M. 2009. Colloidal dispersion of gold nanorods: Historical background, optical properties, seed-mediated synthesis, shape separation and self-assembly. *Materials Science and Engineering: R: Reports*, 65(1-3): 1-38.
- Selvakumar, S., Manivasagan, R. & Chinnappan, K. 2012. Biodegradation and decolourization of textile dye wastewater using *Ganoderma lucidum*. *3 Biotech*, 3(1): 71-79.
- Stadtländer, C. 2007. Scanning Electron Microscopy and Transmission Electron Microscopy of Mollicutes: Challenges and Opportunities. *Modern Research and Educational Topics in Microscopy*: 122-131.

- Singh, K. & Arora, S. 2011. Removal of Synthetic Textile Dyes From Wastewaters: A Critical Review on Present Treatment Technologies. *Critical Reviews in Environmental Science and Technology*, 41(9): 807-878.
- Siti, R., Khairunisak, A., Azlan, A. & Noordin, R. 2013. Green Synthesis of 10 nm Gold Nanoparticles via Seeded-Growth Method and its Conjugation Properties on Lateral Flow Immunoassay. *Advanced Materials Research*, 686: 8-12.
- Sytwu, K., Vadai, M. & Dionne, J. 2019. Bimetallic nanostructures: combining plasmonic and catalytic metals for photocatalysis. *Advances in Physics: X*, 4(1): 1619480.
- Thamaphat, K., Limsuwan, P. & Ngotawornchai, B. 2008. Phase Characterization of TiO₂ Powder by XRD and TEM. *Nat. Sci*, (42): 357 - 361.
- Tanabe, I., Ryoki, T. & Ozaki, Y. 2015. The effects of Au nanoparticle size (5–60 nm) and shape (sphere, rod, cube) over electronic states and photocatalytic activities of TiO₂ studied by far- and deep-ultraviolet spectroscopy. *RSC Advances*, 5(18): 13648-13652.
- Thompson, D. 2007. Michael Faraday's recognition of ruby gold: the birth of modern nanotechnology. *Gold Bulletin*, 40(4): 267-269.
- Tran, M., DePenning, R., Turner, M. & Padalkar, S. 2016. Effect of citrate ratio and temperature on gold nanoparticle size and morphology. *Materials Research Express*, 3(10): 105027.
- Turkevich, J., Stevenson, P. & Hillier, J. 1951. A study of the nucleation and growth processes in the synthesis of colloidal gold. *Discussions of the Faraday Society*, 11: 55.
- Yang, Y., Han, S., Zhou, G., Zhang, L., Li, X., Zou, C. & Huang, S. 2013. Ascorbic-acid-assisted growth of high quality M@ZnO: a growth mechanism and kinetics study. *Nanoscale*, 5(23): 11808.
- Yoong, L., Chong, F. and Dutta, B. (2009). Development of copper-doped TiO₂ photocatalyst for hydrogen production under visible light. *Energy*, 34(10), pp.1652-1661.
- Vaiano, V., Iervolino, G., Sannino, D., Murcia, J., Hidalgo, M., Ciambelli, P. & Navío, J. 2016. Photocatalytic removal of patent blue V dye on Au-TiO₂ and Pt-TiO₂ catalysts. *Applied Catalysis B: Environmental*, 188: 134-146.
- Wang, S., Yun, J., Luo, B., Butburee, T., Peerakiathajohn, P., Thaweesak, S., Xiao, M. & Wang, L. 2017. Recent Progress on Visible Light Responsive Heterojunctions for Photocatalytic Applications. *Journal of Materials Science & Technology*, 33(1): 1-22.

- Wang, X., Wang, C., Jiang, W., Guo, W. & Wang, J. 2012. Sonochemical synthesis and characterization of Cl-doped TiO₂ and its application in the photodegradation of phthalate ester under visible light irradiation. *Chemical Engineering Journal*, 189-190: 288-294.
- Wang, Y., Zhao, D., Ma, W., Chen, C. & Zhao, J. 2008. Enhanced Sonocatalytic Degradation of Azo Dyes by Au/TiO₂. *Environmental Science & Technology*, 42(16): 6173-6178.
- Wilhelmy, L. 1850. The law by which the action of acid on cane sugar occurs. *Ann. Phys. Chem*, (81): 413-433.
- Wu, B., Liu, D., Mubeen, S., Chuong, T., Moskovits, M. & Stucky, G. 2016. Correction to "Anisotropic Growth of TiO₂ onto Gold Nanorods for Plasmon-Enhanced Hydrogen Production from Water Reduction". *Journal of the American Chemical Society*, 138(14): 4990-4990.
- Xia, Y. & Yin, L. 2013. Core-shell structured α -Fe₂O₃@TiO₂ nanocomposites with improved photocatalytic activity in the visible light region. *Physical Chemistry Chemical Physics*, 15(42): 18627.
- Xu, H., Zheng, Z., Zhang, L., Zhang, H. & Deng, F. 2008. Hierarchical chlorine-doped rutile TiO₂ spherical clusters of nanorods: Large-scale synthesis and high photocatalytic activity. *Journal of Solid State Chemistry*, 181(9): 2516-2522.
- Xu, W., Jain, P., Beberwyck, B. & Alivisatos, A. 2012. Probing Redox Photocatalysis of Trapped Electrons and Holes on Single Sb-doped Titania Nanorod Surfaces. *Journal of the American Chemical Society*, 134(9): 3946-3949.
- Zaharia, C. & Suteu, D. 2012. *Textile Organic Dyes – Characteristics, Polluting Effects and Separation/Elimination Procedures from Industrial Effluents – A Critical Overview*. Romania: Faculty of Chemical Engineering and Environmental Protection, Romania
- Zhang, H., Yu, P., Yuan, Z. & Luo, Y. 2006. Study of adsorption behavior using activated carbon for removal of colored impurities from 30% caprolactam solution produced by means of SNIA-toluene-technology. *Korean Journal of Chemical Engineering*, 23(3): 455-463.
- Zhao, J., Nguyen, S., Ye, R., Ye, B., Weller, H., Somorjai, G., Alivisatos, A. & Toste, F. 2017. A Comparison of Photocatalytic Activities of Gold Nanoparticles Following Plasmonic and Interband Excitation and a Strategy for Harnessing Interband Hot Carriers for Solution Phase Photocatalysis. *ACS Central Science*, 3(5): 482-488.

- Zhang, Q., Thrithamarassery Gangadharan, D., Liu, Y., Xu, Z., Chaker, M. and Ma, D. (2017). Recent advancements in plasmon-enhanced visible light-driven water splitting. *Journal of Materiomics*, 3(1), pp.33-50.
- Zhang, X., Chen, Y., Liu, R. & Tsai, D. 2013. Plasmonic photocatalysis. *reports on progress in physics*, 76(4): 1-41.